RICE UNIVERSITY

MAGNETIC PAIR CREATION TRANSPARENCY IN GAMMA-RAY PULSARS

by

Sarah A. Story

A THESIS SUBMITTED
IN PARTIAL FULFILLMENT OF THE
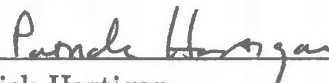REQUIREMENTS FOR THE DEGREE

Master of Science

APPROVED, THESIS COMMITTEE:

Matthew G. Baring, Chairman
Associate Professor

Anthony A. Chan
Professor

Patrick Hartigan
Professor

Houston, Texas

January, 2012

Contents

ABSTRACT

Magnetic pair creation, $\gamma \rightarrow e^+ e^-$, is a key component in polar cap models of gamma-ray pulsars, and has informed assumptions about the still poorly understood radio emission. The Fermi Gamma-Ray Space Telescope has now detected more than 100 γ-ray pulsars, providing rich information for the interpretation of young energetic pulsars and old millisecond pulsars. Fermi observations have established that the high-energy spectra of most of these pulsars have exponential turnovers in the 1-10 GeV range. These turnovers are too gradual to arise from magnetic pair creation in the strong magnetic fields of pulsar inner magnetospheres, so their energy can be used to provide a physically motivated lower bound to the typical altitude of GeV band emission. This work computes pair creation opacities for photon propagation in neutron star magnetospheres. It explores the constraints that can be placed on the emission location of Fermi γ-rays due to single-photon pair creation transparency below the turnover energy, as well as the limitations of this technique. These altitude bounds are typically in the range of 2-6 neutron star radii for the Fermi pulsar sample, and provide one of the few possible constraints on the emission altitude in radio quiet pulsars that do not possess double-peaked pulse profiles.

Chapter 1

INTRODUCTION

1.1 History and Observations

Since the discovery of the first radio pulsars in 1967, the pulsar catalog has grown to more than 2,000 sources. These include 1984 radio pulsars in the most recent ATNF catalog [Manchester et al., 2005], at least 66 x-ray pulsars as of 2006 [Liu, van Paradijs, & van den Heuvel, 2006], and 14 optical pulsars as of 2006 [Shearer, O'Connor, & Tuairisg, 2006]. The most significant early development in high-energy pulsar observations was the launch of the Compton Gamma-Ray Observatory, with the EGRET instrument on board. EGRET was sensitive from 30 MeV to 30 GeV, a new energy window at the time.

EGRET detected seven young to middle-aged γ-ray pulsars, of which six were high-confidence detections and PSR 0656+14 was a marginal detection; the millisecond pulsar J0218+4232 was also detected at a marginal significance level. All of these sources became the subject of intense scrutiny and multiwavelength campaigns. Of particular interest were the relationship between the γ-ray and radio emission, the presence or absence of thermal emission, and the detailed multiwavelength spectrum.

Six of the seven high-confidence pulsars had radio counterparts, while the Geminga pulsar may be radio-quiet within the limits of our detection sensitivity; the low-

frequency detection claimed by Malofeev & Malov [1997] has been questioned by Kassim & Lazio [1999]. Multiwavelength observations showed that the gamma-ray emission appeared to lead the radio peaks in all cases except Geminga and the Crab pulsar (see the review article by Harding [2007] and many others for the state of pulsar observations prior to Fermi). The peaks in the Crab pulsar's folded light curve are aligned in phase for all measured frequencies.

Chandra and XMM-Newton x-ray observations were used to measure surface thermal emission from pulsars (see Zavlin [2007] for an excellent review of these observations). Most of the pulsars for which thermal emission was observed (notably the EGRET pulsars Vela, Geminga, B0656+14, and B1055-52) showed a thermal x-ray spectrum that could be fit by a combination of two blackbodies of different temperatures, possibly with the cooler blackbody corresponding to the majority of the neutron star surface and the hotter blackbody corresponding to a heated polar cap. In the very youngest pulsars, such as the Crab, nonthermal magnetospheric emission completely swamps the thermal emission from the surface.

More recently, the atmospheric Cherenkov telescopes MAGIC and VERITAS have detected pulsed emission from the Crab pulsar, phase-aligned with the peaks in other frequencies, above 25 GeV and 100 GeV respectively [Aleksić et al., 2011, Aliu et al., 2011]. These observations suggested that the shape of the Crab spectrum at the highest energies might be better described by a broken power law than by exponential cutoffs.

EGRET also detected about 200 sources with no clear identification with known source classes. In the years when the Fermi Gamma-Ray Space Telescope was in development, there was a strong debate over how many of the EGRET unidentified sources were actually pulsars. Harding & Muslimov [2004] predicted, based on slot gap arguments, that as many as 2/3 of the 28 unidentified EGRET sources with at least 1 radio pulsar in their EGRET error box might be pulsars. Despite having possible radio associations, these sources did not have enough EGRET photons to search for a periodic γ-ray signal. Other EGRET unidentified sources had pulsar-like spectra, with high spectral curvature and low variability, but no radio counterpart could be found. Except for the very brightest sources, EGRET was not sensitive enough to allow for blind period searches, a process that requires many photons and very long observations, so the possibility that these sources might be Geminga-like pulsars could not be adequately tested.

After the launch of Fermi, many EGRET unidentified sources turned out to be pulsars. The pulsar catalog increased more than tenfold in just two years, from 7 to over 100 at the most recent count. Blind searches, aided by a new time-differencing technique developed by Atwood et al. [2006], have discovered 35 pulsars to date, only four of which were shown to have radio counterparts in follow-up searches [Abdo et al., 2009a, 2010a, Saz Parkinson et al., 2010]. Prior to Fermi, PSR J0218+4232 was the only hint of a γ-ray millisecond pulsar, and it was a marginal detection. Fermi revealed that gamma-ray millisecond pulsars are a significant population with spectral

properties similar to young pulsars.

Fermi's Large Area Telescope (LAT) is sensitive from 30 MeV up to 300 GeV, a range that comfortably includes the pulsar cutoffs at a few GeV measured by EGRET. Newly available information from Fermi included well-measured pulsar spectral energy distributions and much finer resolution in the pulse phase of the pulsars' folded light curves. The new measurements of the spectral cutoffs have helped to settle long-standing physics questions. Better-resolved folded light curves provided new insight into the detailed structure of gamma-ray pulses and allowed for phase-resolved spectroscopy, both of which tie into emission geometry questions; the best example is the extremely bright Vela pulsar [Abdo et al., 2009b, 2010b].

1.2 The Neutron Star Paradigm

In the accepted pulsar picture, pulsars are rapidly rotating neutron stars with mass of the order of the Chandrasekhar mass ($1.44 M_\odot$) and radius of approximately 10 km. The details of the neutron star structure depend on the equation of state, which is not well known. In most models, starting at the surface, one first encounters a crystalline crust of electrons and nuclei. At densities exceeding the critical density for neutron drip (4.3×10^{11} g cm^{-3}), where n-p-e equilibrium is driven in favor of neutrons, an inner crust of nuclei, electrons, and superfluid neutrons forms. The outer and inner crust together are generally less than 1 km thick. Working inward, when the density is greater than nuclear densities ($\rho_{nuc} \approx 2.8 \times 10^{14}$ g cm^{-3}), protons become superfluid

as well; the thickness of this layer depends strongly on the stiffness of the equation of state. At the center of the star, even more exotic forms of condensed matter are believed to exist [Shapiro & Teukolsky, 1983].

Neutron star magnetosphere models generally fall between the extremes of a vacuum dipole, which has analytic solution derived by Deutsch [1955], and a completely pair-flooded force-free magnetosphere, in which all electric fields parallel to the magnetic field lines are shorted out by the plasma. Some amount of plasma must exist in the magnetosphere due to the high drift electric fields induced by the pulsar's rapid rotation, but particle acceleration clearly does occur, so a realistic magnetosphere must be some intermediate model between these two extremes. For examples of such finite-conductivity models, see Kalapotharakos et al. [2011] and Li, Spitkovsky, & Tchekhovskoy [2011].

In an intermediate model containing some plasma, particle acceleration is assumed to occur in "vacuum gaps", plasma-free regions in which an electric field parallel to the magnetic field can persist. In these gaps, the electric field is very strong, and charged particles entering the gap are quickly accelerated to high Lorentz factors. Three specific cases of gap locations and shapes are discussed below.

Particles can be removed from the surface and injected into the acceleration region in one of two ways. First, if the neutron star temperature exceeds the work function for electrons in the crystal lattice, electrons can be liberated from the neutron star surface in that way. If the neutron star is hot enough, it may exceed the ion work

function as well, allowing for free emission of charges of either sign. Second, if a gap exists at the neutron star surface, the gap electric field is easily able to rip charges from the crystal lattice and accelerate them. The curvature photons from this acceleration travel outward and convert to electron-positron pairs in the strong electric and magnetic fields, creating a "pair formation front" above which the electric field is screened and further acceleration cannot take place [Muslimov & Harding, 2004]. This is the picture underpinning polar cap pulsar models.

1.3 Pre-Fermi Modeling

1.3.1 Polar Cap Models

The first polar cap models were created by Sturrock [1971] and Ruderman & Sutherland [1975], and have undergone a great deal of modification since then. The neutron star temperature controls whether both electrons and ions can be pulled off the surface of the star, or electrons only. At lower temperatures, only electrons can escape, a vacuum gap with E parallel to B will develop at the surface, and acceleration and radiation will occur at extremely low altitudes. If the temperature is high enough to overcome the ion work function and allow free emission of both electrons and ions, charges can flow freely along field lines. When the particles radiate and the photons produce pairs, a "pair formation front" will develop, above which the pairs screen the electric field and prevent further acceleration (see Arons [1983] and the slot gap section below). Because acceleration and radiation is occurring at low altitudes where

the magnetic field is strongest, the magnetic pair creation process is extremely efficient at attenuating gamma-rays above the pair creation threshold, which leads to the expectation of a super-exponential cutoff in the gamma-ray spectrum [Daugherty & Harding, 1996]. The primary pair (from magnetic pair creation) is generally created in an excited Landau state, and the synchrotron photons they emit as they drop to the ground state set off a pair cascade, which considerably increases the pulsar's pair luminosity. These high pair multiplicities may be required to power pulsar wind nebulae.

1.3.2   Outer Gap Models

Outer gap models argue that no gaps can exist close to the neutron star, because the high $\mathbf{E} \cdot \hat{\mathbf{B}}$ in any vacuum region would immediately drive rapid pair production until the parallel electric field is shorted out and the gap is filled. However, in the outer magnetosphere, a gap can be created either as a consequence of a solution to the difficult problem of a non-aligned rotating neutron star magnetosphere or by assuming charge flow along the last open field line near the light cylinder [Cheng, Ho, & Ruderman, 1986]. The gap then consists of a stripe of field lines near the last open field line, with a high parallel electric field on the field lines in the center of the gap. The electric field falls to zero both at the outer edge of the gap (the last open field line) and the inner edge (the field line closest to the magnetic pole).

The vacuum gap that produces the particle acceleration, pair production, and

radiation is inferred to occur along the last open field line above the null charge surface (defined by $\vec{\Omega} \cdot \vec{B} = 0$). Romani [1996] defines a gap width w, assumed to be proportional to the γ-ray efficiency, and assumes a constant voltage drop across the vacuum gap and electric fields parallel to the magnetic field. Photons are thus accelerated to high Lorentz factors along the curved field lines and emit curvature photons (see, for example, Chiang & Romani [1994]). Eventually, the emitting electrons reach a constant velocity due to radiation reaction, which produces a spectrum with an exponential cutoff. Hirotani has worked to put the outer gap model on a firmer theoretical basis (see Takata et al. [2006] and Hirotani [2011], for example) by solving the Poisson equation self-consistently.

A major prediction of several outer gap models has been the existence of a spectral component at energies far above the spectral turnover at 1-10 GeV, resulting from inverse Compton scattering [Chiang & Romani, 1994]. Upper limits in the TeV band from atmospheric Cherenkov telescopes proved very constraining to outer gap models. At first glance, then, the detection of pulsed emission from the Crab at energies greater than 100 GeV would appear to be good news for the outer gap models. However, the shape of the Crab's VHE spectrum appears to be inconsistent with a curvature peak plus an inverse Compton peak, and possibly more consistent with a single broken power law over the entire Fermi-MAGIC-VERITAS range [Aliu et al., 2011].

1.3.3 Slot Gap Models

The slot gap picture is basically an extension of the polar cap model to high altitudes, and differs from outer gap models mainly in the location and shape of the vacuum gaps (see Muslimov & Harding [2004]). The pair formation front (see Figure 1.1) develops as in the polar cap model of space charge limited flow. However, narrow vacuum gaps persist from the surface all the way out to the light cylinder along the last open field line due to inefficient pair screening of the electric field, and electrons and positrons can be accelerated through these gaps and continue to produce photons via curvature radiation. The electron Lorentz factors are once again limited by radiation reaction, and like the outer gap, the slot gap can produce single-peaked, double-peaked, or more complex pulse profiles. A purely geometric variant of this model includes emission from both poles (explaining some inter-pulse emission), and is known as the Two-Pole Caustic model [Dyks & Rudak, 2003].

Prior to the launch of Fermi, all of these models were still considered viable. EGRET had detected the turnover in some pulsar SEDs, but only as a few points at the upper limit of its energy range. EGRET data were equally consistent with either an inner magnetosphere or outer magnetosphere model. Razzano & Harding [2007] noted this fact and predicted that Fermi should be able to distinguish between polar cap and outer magnetosphere (slot gap and outer gap) models based on the shape of the spectral turnover. Early Fermi LAT observations of the Vela pulsar showed a simple exponential cutoff [Abdo et al., 2009b], and subsequent observations of Vela

and other pulsars have corroborated this and shown that the simple exponential cutoff is present in both phase-averaged and phase-resolved spectroscopic data [Abdo et al., 2010b]. Observations of the other EGRET pulsars and newly detected Fermi pulsars made it clear that the turnovers in every case were exponential, thus ruling out the polar cap class of models [Abdo et al., 2010a].

1.3.4   Current State of Pulsar High-Energy Emission Modeling

There is now a strong effort underway from both the outer gap and slot gap camps to produce detailed light curve models and attempt to match the vast array of information that the Fermi data provides (see, for example, Watters et al. [2009], Pierbattista et al. [2010], and Harding et al. [2011]). Typically, these calculations involve a Monte Carlo technique and attempt to match the folded gamma-ray light curve, and sometimes also the folded radio light curve and polarization signature, by varying the pulsar inclination angle, the viewing angle, the gap width, and probable emission radii. All these modeling efforts are plagued by a great deal of geometric uncertainty.

Fermi has provided a wealth of detailed data for comparison to these models. Observations of the Vela pulsar [Abdo et al., 2009b], for example, show features such as a third γ-ray peak between the two main peaks that shifts in phase with energy and a decreasing ratio between the heights of the first and second peaks as the energy increases. These features can both challenge and inform γ-ray emission modeling.

In practice, it can be very difficult to say which model is favored by the available
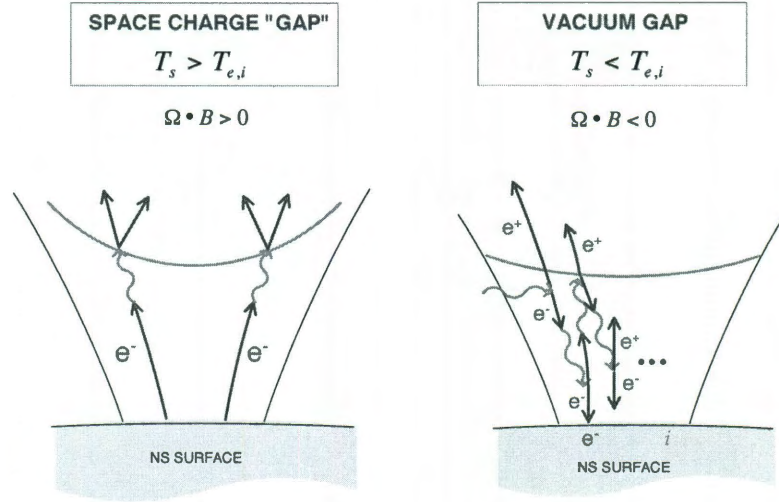
Figure 1.1 : Shape of the pair formation front and accelerating region in polar cap models, from Harding [2007]. The left panel is applicable to the slot gap case, as the PFF extends to high altitudes along the last open field line.

light curves. Fig. 1.3 below shows an example of best fits with the two models for PSR J0030+0451, as calculated in Johnson, Harding, & Venter [2011]. Similarly, in Abdo et al. [2011], fits to PSR J0007+7303 (the CTA1 pulsar) imply that either scenario is possible at slightly different viewing geometries. In these cases, additional constraints from pair creation physics may be useful in narrowing the phase space for solutions.

1.4 Motivation for This Work

Even though pair creation-driven cutoffs do not occur in the Fermi pulsar sample, it is still worthwhile to perform the calculations for pair creation cascades. The fact that super-exponential cutoffs are not observed can be used to place a physical lower bound on the altitude of origin for the high-energy emission. The magnetic pair creation process is strongly height-dependent and should dominate at low altitudes. Since the signature of strong pair creation - a super-exponential cutoff in the spectrum - is not observed, the emission altitude must be high enough that attenuation due to single-photon pair production is not expected. The physical lower bound for the emission height should be considered as a complement to geometric determinations of the emission height from peak separation [Watters et al., 2009] and can help constrain magnetospheric geometry in pulsars without 2 gamma-ray peaks (about 30% of the blind search pulsars, according to Saz Parkinson et al. [2010]). Minimum altitudes from magnetic pair creation are unlikely to help in constraining outer gap models or determining useful lower bounds for millisecond pulsars (because the low millisecond pulsar magnetic fields make magnetic pair creation inefficient).

Furthermore, pair production rates are important in the understanding of pulsar wind nebula energetics. The Goldreich-Julian currents alone cannot carry enough energy to account for pulsar wind nebula luminosities [de Jager, 2007], and to achieve the required energy deposition, there must be prolific pair creation occurring in the pulsar magnetosphere. Single-photon magnetic pair creation is very efficient at low

Light cylinder

≈ 130 stellar radii

Rotation axis

Magnetic field

Outer gap region

Polar cap region

Neutron star

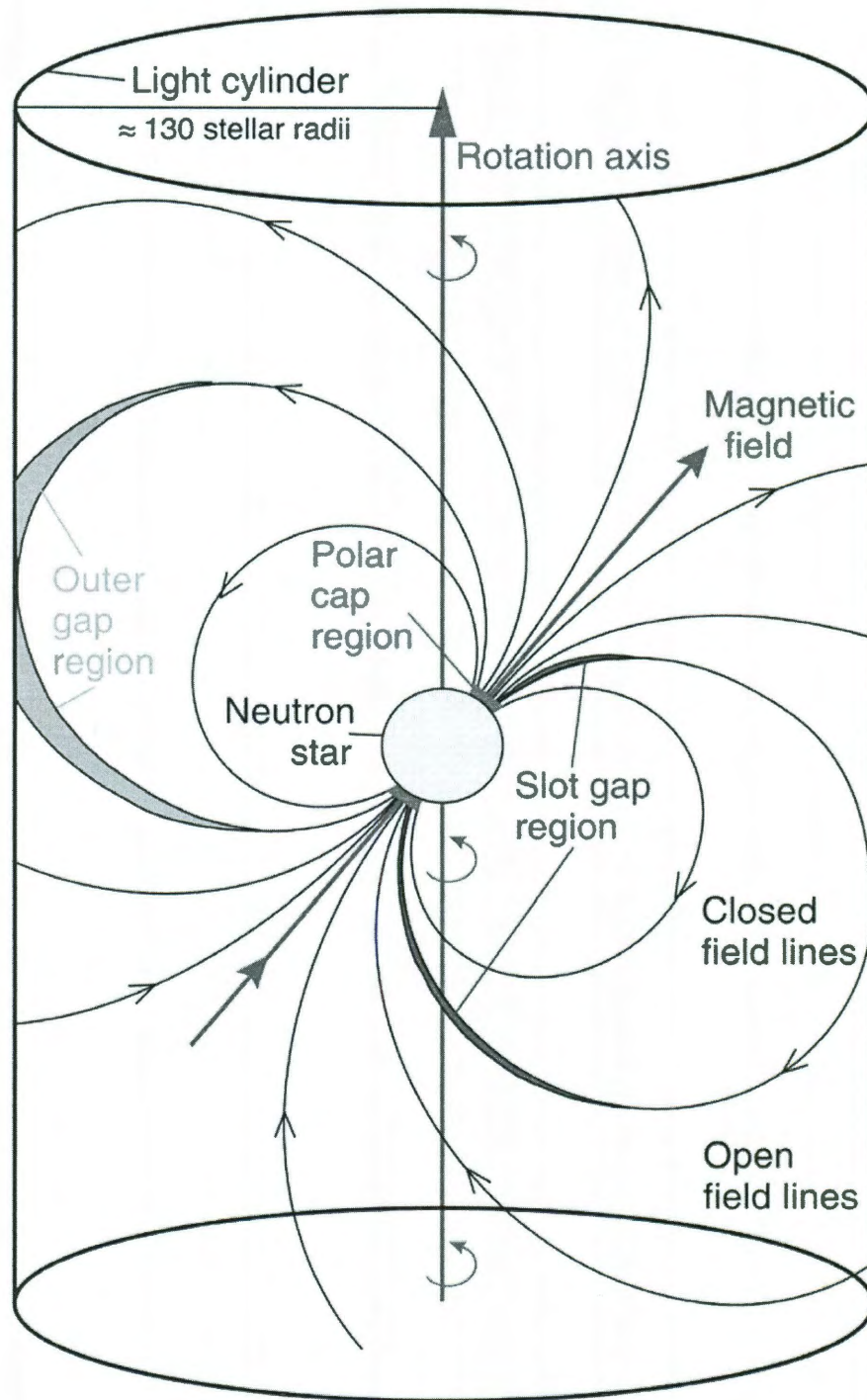Slot gap region

Closed field lines

Open field lines

Figure 1.2 : Diagram showing the emission sites for each of the three gamma-ray emission models discussed above, from Aliu et al. [2008].
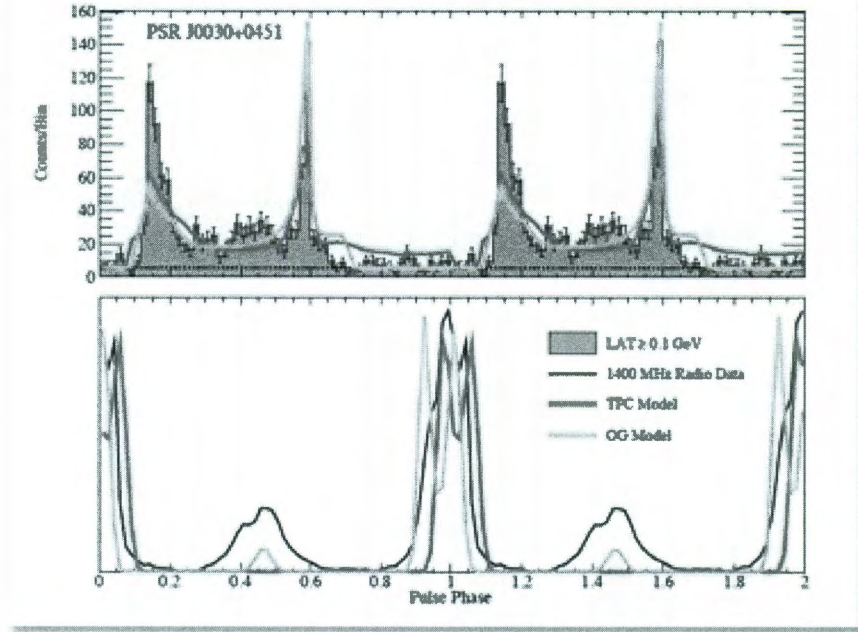
Figure 1.3 : Comparison of best fits to the folded light curve of the millisecond pulsar J0030+0451, for both γ-ray (top) and radio (bottom) emission, from Johnson, Harding, & Venter [2011]. The key fitting parameters are α, the inclination angle between the magnetic axis and the rotation axis, and ζ, the viewing angle between the rotation axis and the line of sight. The pink curves are a slot gap/two-pole caustic model with $\alpha = 73°, \zeta = 57°$, and the green curves are an outer gap model with $\alpha = 81°, \zeta = 66°$. The best fits were calculated with a Markov Chain Monte Carlo technique. For this pulsar, the slot gap model is slightly statistically favored.

altitudes and can produce pair multiplicities approaching those needed to achieve the required energy deposition.

Ho, Epstein, & Fenimore [1990], working on early gamma-ray burst theory, recognized that $\gamma - B$ attenuation posed a major problem for the escape of gamma-rays from the neutron star surface. Their calculations, which ignored general relativistic and rotational aberration effects, showed that for the escape probability to be significant at soft gamma-ray energies, emission must be strongly beamed around the local magnetic field. For the higher-energy gamma-rays seen by Fermi, relativistic beaming guarantees that photons will be emitted essentially parallel to the local magnetic field. In Harding, Baring & Gonthier [1997], although the focus was on photon splitting, the authors carried out single-photon pair production attenuation calculations for comparison purposes. These calculations included GR influences and detailed consideration of threshold effects in the computation of photon attenuation lengths and escape energies. Baring & Harding [2001] produced plots of photon escape energy vs. colatitude of emission for photons originating at the neutron star surface. They also discussed cascading and the conditions under which pair creation (and therefore, arguably, radio emission) should be effectively quenched. Most recently, Lee et al. [2010] tackled the problem of $\gamma - B$ attenuation in detail. Their work, which deals with critical aberration and GR corrections but largely ignores threshold behavior in the pair creation process, produced minimum emission altitudes as a function of photon energy.

The physics that determines the form of the $\gamma - B$ attenuation coefficient is discussed in some detail in section 2. The first attempt to describe this first-order QED process in a manageable form was carried out in the seminal work by Erber [1966], which provided an asymptotic form of the attenuation coefficient. Tsai & Erber [1974] subsequently dealt in detail with the differences in photon polarization modes. Near the pair creation threshold, the simple asymptotic approximations become less accurate. One empirical approximation to threshold behavior can be found in Daugherty & Harding [1983], and an analytic one in the later work of Baring [1988].

In this work, we have taken an analytical approach to the problem of pair creation opacity whenever possible. We present magnetic pair creation transparency conditions as a function of the colatitude and height of emission for photons initially parallel to the local magnetic field. This initial condition is reasonable due to the extremely strong relativistic beaming of radiation from ultra-relativistic primary electrons. We have included, analytically where possible, corrections for threshold conditions on magnetic pair creation [Baring, 1988], gravitational redshift, and general relativistic magnetic field distortion. We provide comparisons with earlier work, including Chang, Chen, & Ho [1996], Gonthier & Harding [1994], Harding, Baring & Gonthier [1997], and Baring & Harding [2001]. Furthermore, the detailed geometry calculations will pave the way for the exploration of other attenuation mechanisms, including $\gamma - \gamma$ attenuation, which is expected to occur at higher altitudes.

Chapter 2

REACTION RATES FOR MAGNETIC PAIR CREATION

Magnetic pair creation is a quantum mechanical process by which a single photon in a strong electromagnetic field converts to an electron and a positron. It has been well understood since the work of Toll [1952] and Klepikov [1954], but is not observed in Earth environments because of the magnetic field strengths required. This process is forbidden in field-free regions due to four-momentum conservation, but in a magnetic field with magnitudes approaching the quantum critical field ($B_{\mathrm{cr}} = m_e^2 c^3/(e\hbar) = 4.413 \times 10^{13}$ Gauss, at which the cyclotron energy equals $m_e c^2$), perpendicular momentum conservation is not required because the excess momentum perpendicular to $\mathbf{B}$ can be absorbed by the field. Magnetic pair creation is first order in the fine structure constant ($\alpha_f = e^2/\hbar c$), with a Feynman diagram with one vertex. The pair-production rate differs markedly for parallel and perpendicular photon polarizations (defined relative to the plane containing the magnetic field vector and the photon trajectory), and has a hard threshold at $\omega = 2m_e c^2/\sin\theta_{kB}$ where the energy available for pair creation is equal to the rest mass energy of the electron-positron pair. In strong magnetic fields, this can be the dominant mode of pair conversion.

When a photon converts to a pair, the electron and positron are generated in ex-

cited Landau levels in the magnetic field. Near the pair creation threshold, only a few energy levels are accessible, and the attenuation rate has a characteristic sawtooth structure, rising to a series of divergent peaks as it approaches the energy of each Landau level from the right (Daugherty & Harding [1983], hereafter DH83; see also Baier & Katkov [2007]). The number of accessible states rises dramatically as the energy increases. The divergences are integrable, so that approximating the attenuation coefficient by averaging over the sawtooth peaks in $\omega_\perp = \omega \sin\theta_{kB}$ is possible, using the proper-time technique developed by Schwinger [1951]. The most commonly used asymptotic approximations were derived by Klepikov [1954], Erber [1966], Sokolov & Ternov [1968], and Tsai & Erber [1974]. These attenuation coefficients take the general form

$$\mathcal{R}^{\mathrm{pp}}_{\|,\perp} = \frac{\alpha_f}{\lambda_c} B \sin\theta_{\mathrm{kB}} \, \mathcal{F}_{\|,\perp}(\omega_\perp, B) \quad , \quad \omega_\perp = \omega \sin\theta_{\mathrm{kB}} \quad , \tag{2.1}$$

where $\lambda = \hbar/m_e c$ is the Compton wavelength over 2π and $\mathcal{F}$ is a dimensionless function specific to the method used to obtain the approximation. Throughout, we will use the scaling convention that B will be dimensionless, scaled to the quantum critical field B_{cr} defined above, and ω will be a dimensionless energy in units of $m_e c^2$. The angle θ_{kB} is the local angle between the photon trajectory $\mathbf{k}$ and the magnetic field vector $\mathbf{B}$. The factor of $\sin\theta_{kB}$ comes from a Lorentz transformation from the frame where $\mathbf{k} \cdot \mathbf{B} = 0$ into the local magnetic frame.

Erber [1966] and Tsai & Erber [1974] derived a simple expression for the function $\mathcal{F}$ by performing a weighted integral over all the possible energies of the created pairs

in the ultra-relativistic limit. These integrals can be evaluated by the method of steepest descents when $\omega_\perp B \ll 1$, which is often the case in pulsar magnetospheres. The asymptotic expressions for $\mathcal{F}$ are then

$$\mathcal{F}_\perp = \frac{1}{2}\mathcal{F}_\parallel = \frac{2}{3}\mathcal{F}_{\text{Erber}} \quad , \quad \mathcal{F}_{\text{Erber}}(\omega_\perp, B) = \frac{3\sqrt{3}}{16\sqrt{2}}\exp\left(-\frac{8}{3\omega_\perp B}\right) \quad , \quad (2.2)$$

for $\omega_\perp \geq 2$. Thus, the attenuation rate increases rapidly with $\sin\theta_{kB}$, the magnetic field strength, and the photon energy. Dimensional arguments with typical photon energies observed from pulsars lead one to expect that the attenuation rate will fall to effectively zero above approximately 10 NS radii from the surface. The expression for $\mathcal{F}_{Erber}$ is a polarization-averaged rate, widely deployed in pulsar calculations, and has been used in the development of polar cap models for radio pulsars (e.g. Sturrock 1971; Ruderman and Sutherland 1975; Daugherty & Harding 1982, 1996). Lee et al. [2010] also used this form for their calculations of minimum altitudes of emission that account for rotation effects.

In both polar cap and outer magnetosphere models, the electrons that radiate curvature γ-rays are accelerated along magnetic field lines to high Lorentz factors. Hence, the γ-rays are relativistically beamed into a tiny cone around the magnetic field lines. All photons therefore start out with very small $\sin\theta_{kB}$, which means they begin their propagation well below the pair conversion threshold. For photons emitted from the surface, this means they must travel a distance s on the order of the field line radius of curvature ρ_c before they will cross threshold, since $\sin\theta_{kB} \sim s/\rho_c$. For the attenuation rate to be appreciable, the exponential of Eq. (2.2) must be

of order unity, represented by $\omega B \sin\theta_{kB} \gtrsim 0.2$. Looking at the threshold condition $(\omega \sin\theta_{kB} > 2)$, we can see that this implies that for magnetic fields $B \ll 0.1 B_{cr}$, pair creation will take place well above threshold, and Eq. (2.2) is adequate. However, for higher magnetic fields $(B \gtrsim 0.1 B_{cr})$, the photon attenuates almost immediately after crossing the threshold, placing it in the regime where the Erber approximation to the attenuation rate diverges dramatically from the exact rate (see Fig. 2.1). For high fields, therefore, it is critically important to obtain a better description of the threshold behavior. Chang, Chen, & Ho [1996], Harding, Baring & Gonthier [1997], and Baring & Harding [2001] all deal with these threshold corrections, but Lee et al. [2010] does not. One can treat the threshold in several different ways, from using the full exact form near threshold (as Chang, Chen, & Ho [1996] did) to the parameterization that Daugherty & Harding [1983] obtain by fitting. We choose to use the analytic result developed by Baring (1988; see also Baring 1991) from detailed asymptotic analysis of the exact pair creation formalism:

$$\mathcal{F}_{B88}\left(\omega_\perp, B\right) = \frac{3\omega_\perp^2 - 4}{2\omega_\perp^2 \left(\omega_\perp + 2\right)^2} \sqrt{\frac{\omega_\perp^2 - 4}{\mathcal{L}(\omega_\perp)\,\phi(\omega_\perp)}} \exp\left\{-\frac{\phi(\omega_\perp)}{4B}\right\} \quad , \quad \omega_\perp \geq 2 \quad ,$$

$$(2.3)$$

for

$$\phi(\omega_\perp) = 4\omega_\perp - \left(\omega_\perp^2 - 4\right)\mathcal{L}(\omega_\perp) \quad , \quad \mathcal{L}(\omega_\perp) = \log_e\left(\frac{\omega_\perp + 2}{\omega_\perp - 2}\right) \quad . \qquad (2.4)$$

Note that this is slightly different from the definition of $\phi(\omega_\perp)$ in Gonthier & Harding [1994]; their definition contained a typographical error. The origin of this analytic result is a modification of the WKB approximation Sokolov & Ternov [1968] applied
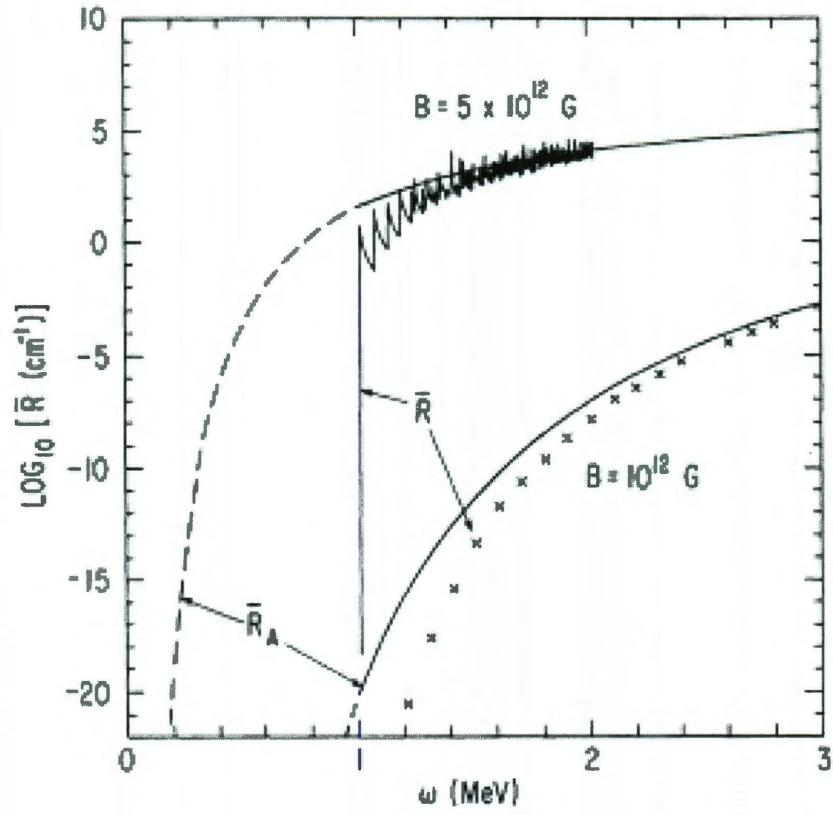
Figure 2.1 : Figure 5 of Daugherty & Harding [1983], showing the exact and asymptotic attenuation coefficients. The attenuation coefficient is plotted against a quantity that we would designate $\omega_\perp/2$ in our notation. The solid curve is the exact coefficient and the dashed curve is the Erber approximation given in Eq. (2.2). Note the divergence of several orders of magnitude near the threshold at $\omega_\perp/2 = 1$.

to the Laguerre functions appearing in the exact $\gamma \to e^+e^-$ rate, to specifically treat created pairs that are mildly-relativistic. This polarization-averaged expression improves the accuracy of the attenuation coefficient by orders of magnitude over the Erber approximation very near the pair creation threshold. In the limit of $\omega_\perp \gg 1$, Eq. (2.3) reduces to the Erber result in Eq. (2.2).

When the magnetic field goes even higher, even these excellent approximations do not provide a good description of near-threshold behavior, and we must treat the

exact sawtooth function. Furthermore, the distinction between the two polarization states becomes important, since the perpendicular state has a higher threshold than the parallel state. In practice, as long as the condition $\omega_\perp B \lesssim 1$ is satisfied, the approximation in Eq. (2.3) is good up to $B \sim 0.5 B_{cr}$ or so. Above that, a further correction to account for the fact that only the lowest Landau levels are energetically accessible near threshold is necessary. We take the same approach as Harding, Baring & Gonthier [1997]; we do an exact treatment for the first accessible state of each polarization and thereafter use the asymptotic expression from Eq. (2.3). This corresponds to calculating the first two peaks of the sawtooth function shown in Fig. 2.1.

The photons in the parallel polarization state access the ground (0,0) state first, where (j, k) denotes the Landau level quantum numbers of the produced pairs. The exact attenuation coefficient for the parallel state is given in Daugherty & Harding [1983], and takes the form

$$\mathcal{F}_\parallel^{\mathrm{pp}} = \frac{2B}{\omega_\perp^2 |p_{00}|} \exp\left(-\frac{\omega_\perp^2}{2B}\right) \quad , \quad \omega_\perp \geq 2 \quad . \tag{2.5}$$

The (0,0) state is inaccessible to perpendicularly polarized photons, and so the first state available is the first excited state, (1,0) and (0,1). These states are summed over to give the perpendicular attenuation coefficient:

$$\mathcal{F}_\perp^{\mathrm{pp}} = \frac{2B\, E_0(E_0 + E_1)}{\omega_\perp^2 |p_{01}|} \exp\left(-\frac{\omega_\perp^2}{2B}\right) \quad , \quad \omega_\perp \geq 1 + \sqrt{1 + 2B} \quad , \tag{2.6}$$

where

$$E_0 = (1 + p_{01}^2)^{1/2} \quad , \quad E_1 = (1 + p_{01}^2 + 2B)^{1/2}$$

for

$$|p_{jk}| = \left[\frac{\omega_{\perp}^2}{4} - 1 - (j + k)B + \left(\frac{(j - k)B}{\omega_{\perp}} \right)^2 \right]^{1/2} \quad ,$$

which describes the magnitude of the momentum parallel to $\mathbf{B}$ of each member of the produced pair in the specific frame where $\theta_{\mathrm{kB}} = \pi/2$, i.e. $\mathbf{k} \cdot \mathbf{B} = 0$. Above $\omega_{\perp} = 1 + \sqrt{1 + 4B}$, which would be the location of the sawtooth peak corresponding to the $(2,0)$ state, we transition to the asymptotic attenuation coefficient. Because the parallel and perpendicular photon polarizations have different pair creation thresholds, it can be important to handle this properly if one is interested in calculating mean free paths for attenuation, especially at $B \gtrsim B_{cr}$. In practice, the photon usually attenuates very quickly after crossing threshold, so that the polarization-dependent attenuation rate behaves effectively like a step function in this regime. The implication is that it does not matter much for near-critical or supercritical fields whether one uses the exact attenuation rate or any of the various approximations, as long as the kinematic thresholds are treated precisely. In contrast, for significantly sub-critical fields, pair creation usually takes place well above the kinematic thresholds, so the asymptotic expressions are entirely appropriate. In Section 3, we will show that in sub-critical fields, quantities like the attenuation length and escape energy are insensitive to polarization.

Chapter 3

PAIR CREATION IN STATIC, FLAT SPACETIME MAGNETOSPHERES

Although general relativistic effects are expected to be important near the neutron star surface, we can glean some important insights from considering the case of photon attenuation in a dipole magnetic field in flat spacetime. This was the case dealt with by Ho, Epstein & Fenimore (1990), Chang, Chen & Ho (1996) and Lee et al. (2010), among others, and we compare our results to theirs. Furthermore, the analytic behavior of the optical depth function is clearest in flat spacetime with no aberration. General relativistic and aberration influences will perturb these results, but the flat spacetime case in the absence of rotation will provide a useful limit against which to check the more complex calculations. We will also confirm a result of Zhang & Harding (2000; see also Lee et al. 2010), which indicates that in flat spacetime the photon escape energy scales with emission altitude r as $r^{5/2}$, in the absence of rotational aberration effects.

To assess the importance of single-photon pair creation in pulsars, we compute pair attenuation lengths and escape energies as functions of the photon emission location, i.e. altitude and colatitude, and also as functions of the energy observed at infinity. Following Gonthier & Harding (1994) and Harding, Baring & Gonthier (1997), the optical depth for pair creation out to some path length l, integrated over the photon

trajectory, is

$$\tau(l) \; = \; \int_0^l \mathcal{R} \, ds \quad , \tag{3.1}$$

where $\mathcal{R}$ is the attenuation coefficient, in units of cm^{-1}, as expressed in general form

in Eq. (2.1). Also, s is the path length along the photon trajectory in the local

inertial frame; in flat spacetime, all such inertial frames along the photon path are

coincident. With this construct, the probability of survival along the trajectory is

$\exp\{-\tau(l)\}$, and the criterion $\tau(l) = 1$ establishes a value of $l = L$ that is termed

the *attenuation length*. A photon will be able to escape the magnetosphere entirely

if $\tau(\infty) < 1$. In general, this will only be possible for photon energies below some

critical value ε_{esc}, at which $\tau(\infty) = 1$; this defines the *photon escape energy* ε_{esc}

as in Harding, Baring & Gonthier (1997) and Baring & Harding (2001). It is the

strongly increasing character of the pair conversion functions in Eqs. (2.2) and (2.3),

as functions of energy ω, that guarantees magnetospheric transparency at $\varepsilon < \varepsilon_{\text{esc}}$.

Observe that these formal definitions apply both to flat spacetimes here, and general

relativistic ones in Section 4.

The geometry for general spacetime trajectories used in the computation of τ

is illustrated in Fig. 3.1. While slight curvature in the photon path is depicted

so as to encapsulate the general relativistic study in Sec. 4, this curvature can be

presumed to be zero for the present considerations of flat spacetime. Each of the

angles in this diagram can be defined once the emission colatitude θ_e and emission

altitude $r_e = hR_{\text{NS}}$ are specified. The instantaneous colatitude θ with respect to the
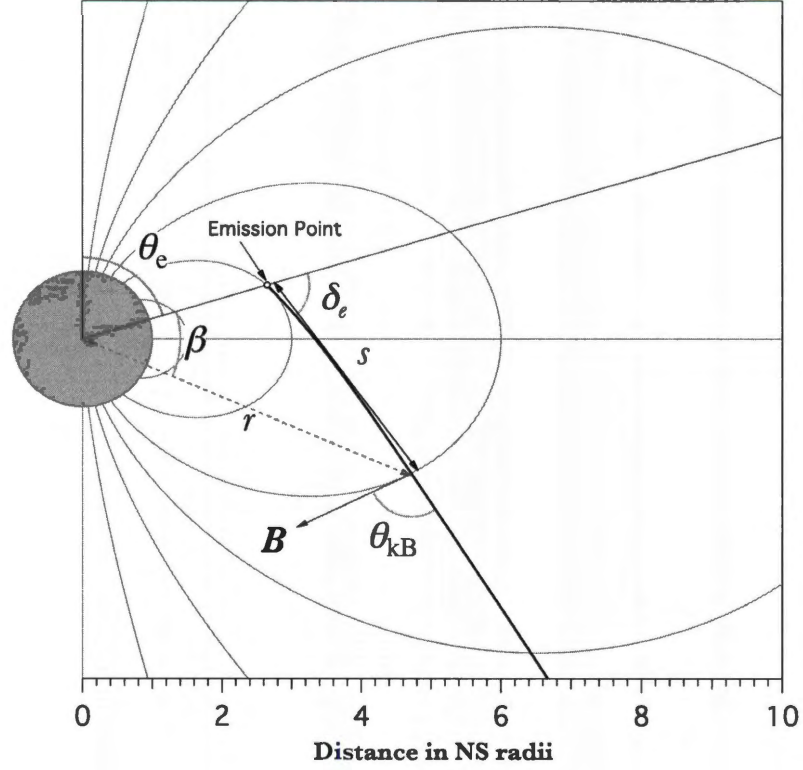
Figure 3.1 : The photon propagation geometry in a dipole magnetic field, representing either curved or flat spacetimes, the latter being for straight line propagation. The photon emission point is defined by the altitude of emission $r_e = hR_{\mathrm{NS}}$ and the emission colatitude θ_e. At any location along the photon path, $\mathbf{k}$ is the photon momentum vector, and $\mathbf{B}$ is the local magnetic field vector; the angle between these two vectors is θ_{kB}, given in Eq. (3.8). All such locations are defined by the propagation angle β, with the radial position r relative to the center of the neutron star, and the distance s from the point of emission, being described by Equations (3.5) and (3.7), respectively.

magnetic axis is

$$\theta = \beta + \theta_e \quad . \tag{3.2}$$

This defines the propagation angle β, which is the angle between the radial vector at the time of emission and the radial vector at the present photon position. The photon trajectory initially starts parallel to the magnetic field, since gamma-rays in pulsars are necessarily emitted by ultra-relativistic electrons that move basically along field lines. Standard models of electron acceleration invoke electrostatic potentials parallel to the local **B** (e.g. Sturrock 1971; Ruderman & Sutherland 1975; Daugherty & Harding 1982), and velocity drifts across **B** due to pulsar rotation are generally much smaller than c for young gamma-ray pulsars. Accordingly, gamma-rays produced by primary electrons of Lorentz factor γ_e are beamed to within a small Lorentz cone of half angle $\sim 1/\gamma_e$ centered along **B**. This restriction conveniently simplifies the trajectory parameter space, so that the angle between the radial direction and the photon trajectory at the point of emission, δ_e (Gonthier & Harding 1994 name this δ_0), is determined only by the colatitude θ_e at the point of emission. The magnetic field vector at any point in a flat spacetime dipole magnetosphere is given by

$$\mathbf{B} = \frac{B_p R_{\mathrm{NS}}^3}{2r^3} \left\{ 2\cos\theta\,\hat{r} + \sin\theta\,\hat{\theta} \right\} \quad . \tag{3.3}$$

where B_p is the surface polar magnetic field, i.e., that at $r = R_{\mathrm{NS}}$ and $\theta = 0$. The geometry of Fig. 3.1 then simply sets

$$\tan\delta_e = \frac{1}{2}\tan\theta_e \quad . \tag{3.4}$$

This result is, of course, independent of the altitude of emission. One remaining piece of the geometry is the relationship between the altitude along the photon path, and the angle β. This is simply derived using the trigonometric law of sines. Given δ_e, the dimensionless distance from the center of the neutron star $\chi = r/r_e$, scaled by the altitude of emission, satisfies

$$\chi \equiv \frac{r}{r_e} = \frac{\sin \delta_e}{\sin(\delta_e - \beta)} \quad . \tag{3.5}$$

This is the locus of a straight line in polar coordinates, and it is trivially determined that $\beta \to \delta_e$ as $r \to \infty$. The photon momentum vector $\mathbf{k}$ along this path satisfies $\hat{\mathbf{k}} \equiv \mathbf{k}/\omega = \cos(\delta_e - \beta)\hat{r} + \sin(\delta_e - \beta)\hat{\theta}$.

For flat spacetime geometry with no aberration influences, it is convenient to restate the optical depth integral in Eq. (3.1) using the propagation angle β as the integration variable:

$$\tau(l) = \frac{\alpha_f}{\lambda_c} \int_0^{\beta(l)} B \sin \theta_{\mathrm{kB}} \, \mathcal{F}(\omega_\perp, B) \frac{ds}{d\beta} \, d\beta \quad . \tag{3.6}$$

The propagation distance s is easily found using the trigonometric law of sines, and thereby yields the change of variables Jacobian $ds/d\beta$ in Eq. (3.6):

$$s = \frac{r_e \sin \beta}{\sin(\delta_e - \beta)} \quad \Rightarrow \quad \frac{ds}{d\beta} = \frac{r_e \sin \delta_e}{\sin^2(\delta_e - \beta)} \quad . \tag{3.7}$$

Therefore, the relationship for $\beta(l)$ is the inversion of Eq. (3.7) for $s = l$, i.e., $\tan \beta = \sin \delta_e / (\cos \delta_e + r_e/l)$. The integrand in Eq. (3.6) includes a dependence on the angle θ_{kB} between the photon trajectory and the local magnetic field, particularly

through the attenuation coefficient function $\mathcal{F}$. The photons start with $\theta_{\mathrm{kB}} = 0$, and this angle increases at first linearly as the photon propagates outward. The angle θ_{kB} is given geometrically by

$$\sin\theta_{\mathrm{kB}} \;=\; \frac{|\mathbf{k} \times \mathbf{B}|}{|k|.|B|} \;=\; \frac{\hat{k}_r B_\theta - \hat{k}_\theta B_r}{|B|} \;=\; \frac{\sin\theta\cos(\delta_e - \beta) - 2\cos\theta\sin(\delta_e - \beta)}{\sqrt{1 + 3\cos^2\theta}} \tag{3.8}$$

at every point along the photon's path. Using Eq. (3.4) simply demonstrates that the right hand side of this expression approaches zero as $\beta = \theta - \theta_e \to 0$. Note also, that forming $\cos\theta_{\mathrm{kB}}$, using Eq. (3.5) one can show routinely that this result is equivalent to Eq. (5) of Baring & Harding (2007). In the limit of small colatitudes near the magnetic axis, one simply derives $\sin\theta_{\mathrm{kB}} \approx 3\beta/2$, which can be combined with $r/r_e \approx 1 + 2\beta/\theta_e$ to yield $\theta_{\mathrm{kB}} \approx 3\theta_e(r/r_e - 1)/4$. This dependence closely approximates the low altitude values for θ_{kB} in flat spacetime exhibited in Fig. 5a of Gonthier & Harding (1994). This completes the general formalism for pair creation optical depth determination in Minkowski metrics.

3.1 Optical Depth for Emission Near the Magnetic Axis

In order to better understand the complicated optical depth integral, it is instructive to consider the case of a photon emitted at very small colatitudes. This situation is representative of much of the relevant parameter space for gamma-ray pulsars. For these photons emitted very close to the magnetic axis, β and θ_e are small. In this limit, we have the approximations

$$B \;\approx\; \frac{B_p(\delta_e - \beta)^3}{h^3\delta_e^3} \quad , \quad \sin\theta_{\mathrm{kB}} \;\approx\; \frac{3}{2}\beta \tag{3.9}$$

for $r_e = hR_{\text{NS}}$. We also have $ds/d\beta \approx r_e\delta_e/(\delta_e - \beta)^2$ using Eq. (3.7), with $\delta_e \approx \theta_e/2$. These results can be inserted into Eq. (3.6), and the integration variable changed to $x = \beta/\delta_e$, yielding an approximation for the optical depth in axial locales:

$$\tau(l) \approx \frac{3\theta_e}{4} \frac{B_p}{h^2} \frac{\alpha_f R_{\text{NS}}}{\lambda} \int_{8/(3\theta_e\varepsilon)}^{x_+} x(1-x)\,\mathcal{F}\left(\frac{3}{4}\varepsilon\theta_e x, \frac{B_p}{h^3}[1-x]^3\right) dx \;, \quad x_+ = \frac{l}{l + hR_{\text{NS}}} \;.$$

$$(3.10)$$

This form is applicable to any choice of the pair conversion function $\mathcal{F}$. Observe the correspondence $\omega \to \varepsilon$. The lower limit defines the threshold condition, so that if $\varepsilon\theta_e \leq 8/3$, propagation in flat spacetime out of the magnetosphere never moves the photon above the pair threshold at $\omega_\perp = 2$, and $\tau = 0$ over the entire photon trajectory. For the particular choice of Erber's (1966) attenuation coefficient in Eq. (2.2), the integral for the optical depth assumes a fairly simple form:

$$\tau(l) \approx \frac{9\sqrt{3}\,\theta_e}{64\sqrt{2}} \frac{B_p}{h^2} \frac{\alpha_f R_{\text{NS}}}{\lambda} \int_{8/(3\theta_e\varepsilon)}^{x_+} x(1-x)\,\exp\left\{-\frac{32h^3}{9\varepsilon B_p\theta_e}\frac{1}{x(1-x)^3}\right\} dx \;. \quad (3.11)$$

If one considers emission points at different altitudes along a particular field line near the magnetic axis, then for a footpoint colatitude θ_f for this field line, $\theta_e \approx \theta_f\sqrt{h}$ gives the altitude dependence of the emission colatitude. This case corresponds to altitude variations for a pulsar whose rotational period fixes the last open field line, the putative site of gamma-ray emission. The escape energy ε_{esc} can be computed by setting $\tau(\infty) = 1$, for which $x_+ \to 1$. Imposing this $\tau(\infty) = 1$ criterion, and presuming $\varepsilon\theta_e \gg 1$ in Eq. (3.11), yields the approximate altitude dependence

$$\varepsilon_{\text{esc}} \propto h^{5/2} \qquad\qquad (3.12)$$

for the escape energy. This is a flat spacetime result for near polar axis locales that was identified by Zhang & Harding (2000; see also Lee, et al. 2010). Deviations from this simple altitude dependence arise when (i) the footpoint colatitude θ_f is not sufficiently small, (ii) the pair creation conversion occurs not very fair from the $\omega_\perp = 2$ threshold, and (iii) down near the stellar surface where general relativistic effects modify the values of ω, B and θ_{kB}.

For significantly sub-critical surface polar magnetic fields B_p, a complete asymptotic expression for the optical depth after propagation to high altitudes can be determined using the method of steepest descents to compute the integral for $\tau(l)$, since the integrand in Eq. (3.11) is exponentially sensitive to values of x. The exponential realizes a very narrow peak at $x = 1/4$, so that for $l \to \infty$ and $x_+ = 1$

$$\tau(l) \approx \frac{3^6}{2^{19}} \left(\frac{3\pi\varepsilon B_p^3 \theta_f^3}{2h^{11/2}} \right)^{1/2} \frac{\alpha_f R_{NS}}{\lambda} \exp\left\{ -\frac{2^{13}h^{5/2}}{3^5 \varepsilon B_p \theta_f} \right\} \quad . \tag{3.13}$$

This result actually applies for any $x_+ > 1/4$, i.e. when $l \gtrsim hR_{NS}/3$. It is independent of l since the integrand has peaked and has shrunk to very small values when x exceeds $1/4$ by a significant amount. Again setting $\tau(\infty) = 1$, and taking logarithms, the escape energy ε_{esc} satisfies

$$\varepsilon_{esc} = \frac{2^{13}h^{5/2}}{3^5 B_p \theta_f} \left\{ \log_e\left(\frac{3^6}{2^{19}} \frac{\alpha_f R_{NS}}{\lambda} \right) + \frac{1}{2}\log_e \frac{3\pi\varepsilon_{esc}B_p^3\theta_f^3}{2h^{11/2}} \right\} \quad . \tag{3.14}$$

While an exact solution for ε_{esc} must be determined numerically from this transcendental equation, the second logarithmic term on the right is only weakly dependent on its arguments. Therefore, to a good approximation, one can infer that $\varepsilon_{esc} \propto 1/B_p$

and $\varepsilon_{\mathrm{esc}} \propto 1/\theta_f$, both of which emerge due to the presence of the factor $\omega_\perp B$ in the argument of the exponential in Erber's asymptotic form.

The same protocol can be adopted for pair conversion rates that include threshold modifications, specifically Eq. (2.3). In this case, as the counterpart of Eq. (3.10) we have

$$\tau(l) \approx \frac{3\theta_e}{4} \frac{B_p}{h^2} \frac{\alpha_f R_{\mathrm{NS}}}{\lambda} \int_{8/(3\theta_e\varepsilon)}^{x_+} x(1-x) \mathcal{F}_{\mathrm{B88}} \left(\frac{3}{4} \varepsilon\theta_e x, \frac{B_p}{h^3} [1-x]^3 \right) dx \quad , \qquad (3.15)$$

again for $x_+ = l/(l + hR_{\mathrm{NS}})$. We can neaten this up a bit more by making the substitution $\lambda = 3\theta_e\varepsilon/8 \geq 1$. The argument of the exponential is of the form $h^3 q(x, \lambda)/B_p$ where

$$q(x, \lambda) \equiv \frac{\phi(x/\lambda)}{4(1-x)^3} = -\frac{2\lambda x}{(1-x)^3} - \frac{(2\lambda x)^2 - 4}{4(1-x)^3} \log_e \left(\frac{\lambda x - 1}{\lambda x + 1} \right) \qquad (3.16)$$

Using the method of steepest descents once again, we take the first derivative of the function in the exponential, and set it equal to zero to find the peak of the function. The solution of $\partial q/\partial x = 0$ is a transcendental function in λ, but it can be numerically approximated to better than 3% by

$$\overline{x} \approx \frac{1}{4} + 0.82\lambda^{-5/3}. \qquad (3.17)$$

Given $\partial q/\partial x = 0$, $q''(x, \lambda)$ can be written in the following form.

$$q''(\overline{x}, \lambda) = \frac{8\lambda \left(\lambda^2 \left(2\overline{x}^3 - 3\overline{x} + 1 \right) - 3\overline{x} + 3 \right)}{(\lambda^2 \overline{x}(\overline{x} + 2) - 3)(1 - \overline{x})^5(\lambda^2 \overline{x}^2 - 1)} \qquad (3.18)$$

The integral is then given approximately, as before, by the method of steepest descents. We will combine some terms and define the quantity Y to clean up the second

derivative term. With some cancellation, we then obtain

$$
\tau \approx \frac{3\theta_e}{4} \frac{B_p}{h^3 B_{cr}} \frac{\alpha_f R_e}{\lambda} \overline{x}(1-\overline{x})^{5/2} \frac{3(\lambda\overline{x})^2 - 1}{(2\lambda\overline{x})^2 \sqrt{2}(\lambda\overline{x}+1)^2}
$$
$$
\times \left[\frac{(\lambda^2\overline{x}^2 - 1)}{4\lambda}\right] \left[\frac{(\lambda^2\overline{x}(\overline{x}+2) - 3)^3}{(\overline{x}+2)}\right]^{1/2} \left[\frac{2\pi B_p}{h^3 B_{cr}|Y|}\right]^{1/2} \qquad (3.19)
$$
$$
\times \exp\left\{-\frac{h^3 B_{cr}}{B_p}\left(\frac{4\lambda}{(1-\overline{x})^2(\lambda^2\overline{x}(\overline{x}+2) - 3)}\right)\right\}
$$

for

$$
Y = 8\lambda\left(\lambda^2\left(1 - 2\overline{x} - 2\overline{x}^2\right) + 3\right) \qquad (3.20)
$$

This agrees with the Erber approximation to high precision in the regime where $\lambda \to \infty$, and exhibits the appropriate threshold behavior. Setting $\tau = 1$ gives a transcendental equation, which can be solved numerically for $\varepsilon_{\mathrm{esc}}$.

3.2 Pair Creation Escape Energies in Flat Spacetime

Numerical solutions of Eq. (3.6) can help us gain a better understanding of where the effects of magnetic pair creation will be the strongest. By specifying surface emission, fixing a surface polar magnetic field B_p and then solving for ε_{esc} as a function of the colatitude of emission θ_e, we obtain the plot shown in Fig. 3.2. We can see that for small colatitude, $\varepsilon_{esc} \propto 1/\theta_e$ and $\varepsilon_{esc} \propto 1/B_p$, as expected from Eq. (3.14). The dashed lines representing the steepest descents approximation in Eq. (3.20) clearly illustrate the remarkable accuracy of this expression over a wide range of colatitudes and subcritical fields. The effects of threshold corrections are also apparent from this figure. For the red $B_p = 1$ curves, the Erber approximation to the attenuation coefficient produces escape energies nearly a factor of 3 below the threshold-corrected result. For lower magnetic fields, pair creation is taking place well above threshold, and the Erber curves are much closer to the threshold-corrected curves.

In comparing with extant flat spacetime computations of escape energies, we also achieve good agreement with Fig. 2 of Ho, Epstein & Fenimore (1990), using the Erber asymptotic form of Eq. (2.2); this matches their chosen attenuation coefficient closely. In this analysis, we assume that photons are always emitted parallel to the magnetic field, so comparison of our results is made to the topmost ($\psi_i = 0$) curve of their Fig. 2, the x-axis of which is equivalent to $\log(\delta_e + \theta_e)$ in our variables. For $B = 2 \times 10^{12}$ Gauss, the apparent difference between our numerics and theirs is less than about 15%, though visual precision in reading this plot limits such an estimate.

For the Erber attenuation coefficient in flat spacetime, multiplying the photon escape energy from a fixed emission altitude and colatitude by the surface polar magnetic field yields an approximately constant result.

If, on the other hand, we fix the surface polar field and the photon energy and calculate the lowest altitude from which photons of that energy can escape to infinity, we can draw a "pair convertosphere" plot like the one in Fig. 3.3. The leaf-shaped curves represent a cross-section through a $\tau = 1$ surface that is symmetric about the magnetic axis. Inside the surface, to a first approximation, all photons of the labeled energy will convert to pairs. Outside the surface, photons can escape and be detected. At a fixed colatitude, a higher altitude of emission results in a higher escape energy (corresponding to shifting the curves in Fig. 3.2 up in energy). In a Minkowski metric, all of these minimum altitude curves drop to zero at the magnetic pole; GR and aberration will force them to higher altitudes. Rotational aberration, which will be considered in a separate work, introduces an azimuthal asymmetry about the magnetic axis for an inclined pulsar and distorts the shape of the surfaces.
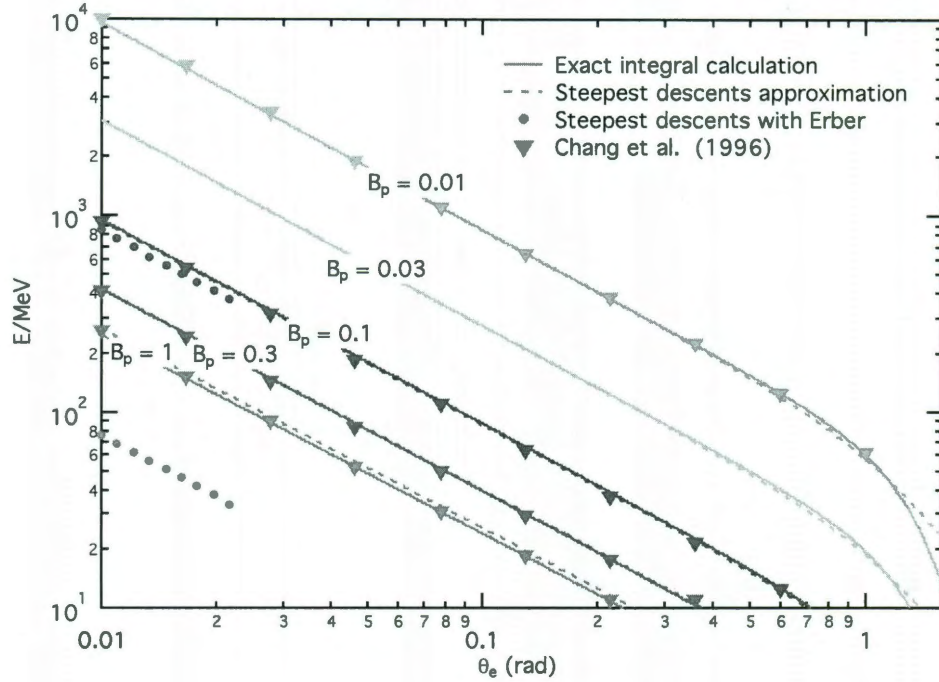
Figure 3.2 : The maximum energy $\varepsilon_{\mathrm{esc}}$ of photons emitted from the neutron star surface ($h = 1$) that can escape to infinity in flat spacetime, plotted as a function of emission colatitude. The curves are labeled with the surface polar magnetic field, B_p , scaled by the quantum critical field. Solid curves represent results for $\tau(\infty) = 1$ using the integral calculation of the optical depth in Eq. (3.10). This determination employs polarization-averaged forms for $\mathcal{F}$ that include the first two "sawtooth" peaks in the exact attenuation coefficient formula of Daugherty and Harding (1983), and at higher $\omega_\perp$ uses the approximation derived by Baring (1988); see Sec. 2 for details. Dashed lines represent the steepest descents approximation in Eq. 28, and the shorted dotted lines depict the asymptotic form obtained using Erber's (1966) reaction rate. Triangles are taken from the computations illustrated in Fig. 2 of Chang et al. (1996), for comparison. The steepest descents approximation remains extremely good out to fairly high colatitudes, and begins to diverge slightly from the exact calculation at the critical field, when a more precise treatment of the multitude of peaks is warranted.
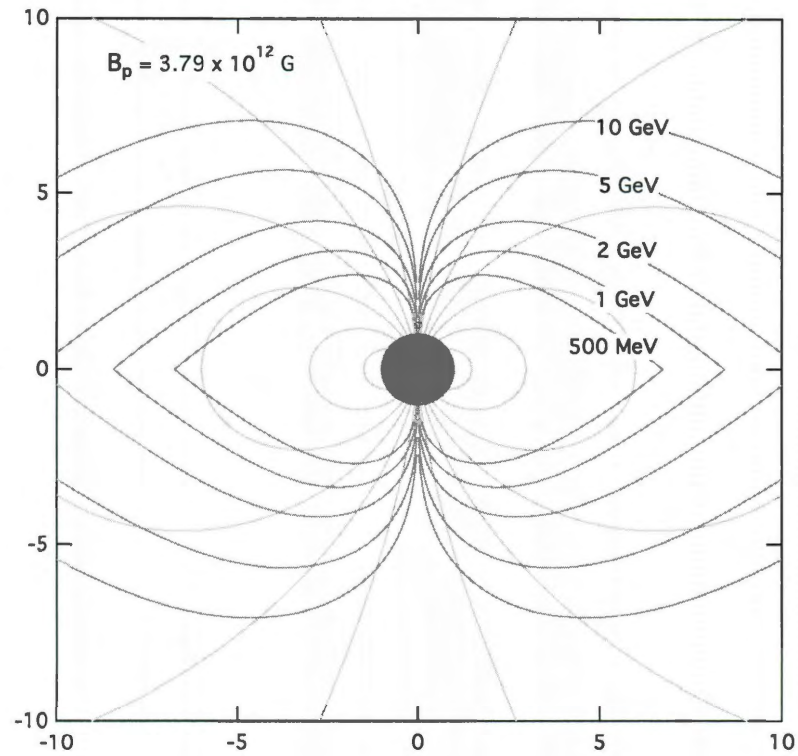
Figure 3.3 : "Pair convertosphere" diagram for a pulsar with the same magnetic field as the Crab, flat spacetime and no rotation. Each green curve represents the lowest possible emission point at a given colatitude for a photon of a given energy, below which magnetic pair creation would attenuate the photon before it could escape from the neutron star magnetosphere. The scale is neutron star radii, with the radius 1 circle in the center representing the neutron star, and pink curves show magnetic field lines. GR effects alter these curves only very near the neutron star surface.

Chapter 4

GENERAL RELATIVISTIC EFFECTS

Our overall approach to calculating curved spacetime effects on photon attenuation will be to integrate the optical depth over the path length in the local inertial frame (hereafter LIF), with all magnetic fields, angles, energies, and distances computed in that frame. In general, we will use the definitions for curved spacetime quantities from Gonthier & Harding [1994] (hereafter GH94), with the notation altered slightly for clarity. Our starting point is again Eq. (3.1), therefore requiring specification of the quantities B, ω and θ_{kB} in the LIF. The blueshift of the photon energy in the LIF from its value $\varepsilon \equiv \omega_\infty$ at infinity (i.e. as observed) can be accounted for with the simple correction

$$\omega \;=\; \frac{\varepsilon}{\sqrt{1-\Psi}} \quad , \quad \Psi \;=\; \frac{r_s}{r} \;\equiv\; \frac{2GM}{c^2 r} \tag{4.1}$$

at radius r, where $r_s = 2GM/c^2$ is the Schwarzschild radius of a neutron star of mass M. The introduction of the dimensionless parameter Ψ to describe the radial position will expedite the path length integration in curved spacetime constructs; we will use it as our integration variable instead of β in Eq. (3.6), approximately equivalently to the approach of GH94. The emission altitude r_e will be prescribed by $\Psi_e = r_s/r_e < 1$. Note that throughout, we will adopt the convention that ε will denote the dimensionless photon energy as seen by an observer, and ω will signify

that in the LIF.

The general relativistic form of a dipole magnetic field in a Schwarzschild metric was developed in Wasserman & Shapiro [1983]. It is also expressed in Eq. (21) of Gonthier & Harding [1994] in the LIF in terms of the coordinates r and θ for an observer at infinity:

$$
\begin{aligned}
\mathbf{B}_{GR} \;=\; & -3\frac{B_p\cos\theta}{r_s^2 r}\left[\frac{r}{r_s}\log_e\left(1-\frac{r_s}{r}\right)+1+\frac{r_s}{2r}\right]\hat{r} \\
& +3\frac{B_p\sin\theta}{r_s^2 r}\left[\left(\frac{r}{r_s}-1\right)\log_e\left(1-\frac{r_s}{r}\right)+1-\frac{r_s}{2r}\right]\frac{\hat{\theta}}{\sqrt{1-r_s/r}} \quad .
\end{aligned}
\tag{4.2}
$$

In flat spacetime, where $r_s \ll r$, B_p represents the surface polar field at $\theta = 0$. It is more convenient to write this in terms of the scaled inverse radius $\Psi = r_s/r$. To this end we define the functions

$$
\begin{aligned}
\xi_r(x) \;&=\; -\frac{1}{x^3}\left[\log_e(1-x)+x+\frac{x^2}{2}\right] \\
\xi_\theta(x) \;&=\; \frac{1}{x^3\sqrt{1-x}}\left[(1-x)\log_e(1-x)+x-\frac{x^2}{2}\right] \quad .
\end{aligned}
\tag{4.3}
$$

Then, the curved spacetime dipole field is expressed via

$$
\mathbf{B}_{GR} \;=\; 3\frac{B_p\Psi^3}{r_s^3}\left\{\xi_r(\Psi)\cos\theta\,\hat{r}+\xi_\theta(\Psi)\sin\theta\,\hat{\theta}\right\} \quad .
\tag{4.4}
$$

In flat spacetime, where $\Psi \ll 1$, the leading terms of the Taylor series expansion yield $\xi_r(\Psi) \approx 1/3$ and $\xi_\theta(\Psi) \approx 1/6$, so that then Eq. (4.4) reproduces the familar result in Eq. (3.3) in the absence of general relativity. The magnitude of the general

relativistic field is then

$$B_{GR} = 3\frac{B_p\Psi^3}{r_s^3}\sqrt{[\xi_r(\Psi)]^2\cos^2\theta + [\xi_\theta(\Psi)]^2\sin^2\theta} \quad ; \qquad (4.5)$$

this will be employed in the quantum pair creation rates in the local inertial frame. The ratio of Eq. (4.5) for altitudes near the surface to its flat spacetime value (i.e., $\Psi \to 0$) inferred from Eq. (3.3) reproduces the ratio plotted in Fig. 5c of GH94.

The trajectory of a photon emitted from a point in a neutron star magnetosphere will be curved in the frame of an observer at infinity, though for cases of emission near the polar cap, this is generally small (see Baring & Harding [2001]). Here we incorporate the influence of the slight curvature in the path, so that calculating $\sin\theta_{\rm kB}$ becomes a slightly more complicated exercise than it was in the flat spacetime approximation. First, the photon is emitted parallel to the magnetic field in the field frame. This fixes δ_e, the initial angle between the photon trajectory and the radial direction (depicted in Fig. 3.1):

$$\sin\delta_e \equiv \left.\frac{B^{\hat\theta}}{B}\right|_{r=R_e} = \frac{\sin\theta_e\,\xi_\theta(\Psi_e)}{\sqrt{\cos^2\theta_e\,[\xi_r(\Psi_e)]^2 + \sin^2\theta_e\,[\xi_\theta(\Psi_e)]^2}} \quad . \qquad (4.6)$$

When $\Psi_e \ll 1$, this reduces to Eq. (3.4), though in general, since $\xi_\theta(\Psi_e)/\xi_r(\Psi_e) \approx 1/2 + \Psi_e/8 + O(\Psi_e^2)$ in this limit, it is easily seen that spacetime curvature increases δ_e for proximity to the magnetic pole. This effect is illustrated in Figure 3b of GH94. The photon's trajectory at infinity emerges parallel to a line drawn from the center of the star, displaced from it by a distance b. This impact parameter b is proportional to the ratio of two conserved quantities of the unbound photon orbit,

the orbital angular momentum and the energy; consult Pechenick, Ftaclas & Cohen [1983] or Chapter 8 of Weinberg [1972] for illustrations of such orbits. Scaling b by the Schwarzschild radius, as we have with r, introduces a new trajectory parameter $\Psi_b = r_s/b$ that can be related to Ψ_e and δ_e via

$$\Psi_b = \frac{\Psi_e}{\sin \delta_e} \sqrt{1 - \Psi_e} \equiv \Psi_e \sqrt{(1 - \Psi_e) \left\{ 1 + [\xi(\Psi_e)]^2 \cot^2 \theta_e \right\}} \quad , \qquad (4.7)$$

where

$$\xi(\Psi) = \frac{\xi_r(\Psi)}{\xi_\theta(\Psi)} \quad . \qquad (4.8)$$

The first identity in Eq. (4.7) is derived from Eq. (17) of GH94, who use the notation δ_0 for δ_e. Observe that the impact parameter can be smaller than the Schwarzschild radius for almost radial trajectories initiated near the magnetic polar axis (setting $\sin \delta_e \ll 1$), so Ψ_b can assume values well in excess of unity where the orbit is a capture one, if reversed. Inserting Eq. (4.6) yields Ψ_b purely as a function of the emission altitude (i.e. Ψ_e) and colatitude θ_e, and derives the second identity in Eq. (4.7), with $0 \leq \xi(\Psi) \leq 2$ on $0 \leq \Psi \leq 1$. This form is needed for the photon trajectory computation, an integral expression for which is given in Eq. (11) of GH94:

$$\theta(\Psi) \equiv \theta_e + \Delta\theta = \theta_e + \int_\Psi^{\Psi_e} \frac{d\Psi_r}{\sqrt{\Psi_b^2 - \Psi_r^2(1 - \Psi_r)}} \quad , \qquad (4.9)$$

expressing the functional dependence $\theta(r)$, as viewed by an observer at infinity. An alternative version of this can be obtained from Eq. (8.5.6) of Weinberg [1972]; see also Misner, Thorne & Wheeler [1973]. Since $\Psi \leq \Psi_e$ in this construction, as the photon propagates out from the star, then the change in colatitude $\Delta\theta$ is necessarily

positive as the altitude r increases. Observe that $\Psi_b^2 > \Psi_e^2(1 - \Psi_e)$ from the second identity in Eq. (4.7) so that the argument of the square root in the integrand of Eq. (A.1) is positive-definite. In the case of a neutron star, generally $\Psi_e \lesssim 0.4$, and the integral in Eq. (A.1) can be approximated extremely accurately by an analytic form, for non-equatorial emission colatitudes $\theta_e \lesssim \pi/4$; see the Appendix for details. This expedient step removes the trajectory integral from consideration, and speeds up optical depth computations immensely. In the flat spacetime limit, $\Psi_e \ll 1$, the integral for the trajectory in Eq. (A.1) can be expressed analytically by replacing the argument of the square root in the denominator by $\Psi_b^2 - \Psi_r^2$. Then, forming $\sin\Delta\theta$, the result can be inverted to solve for Ψ and thereby find the locus for the trajectory:

$$\Psi = \Psi_b \sin\left(\theta_e - \theta - \arcsin\frac{\Psi_e}{\Psi_b}\right) \quad . \tag{4.10}$$

This is a polar coordinate form for a straight line, and is easily shown to be equivalent to Eq. (3.5) using the limiting form $\Psi_b \approx \Psi_e\sqrt{1 + 4\cot^2\theta_e} \approx \Psi_e/\sin\delta_e$ when $\Psi_e \ll 1$.

Given emission locale coordinates (Ψ_e, θ_e), for any subsequent position (Ψ, θ) along the curved trajectory, we can determine the angle θ_{kB} of the photon momentum to the local field direction, in the LIF. This is simply done by forming a cross product between the photon momentum $\mathbf{k}_{GR}$ and $\mathbf{B}_{GR}$ using Eq. (4.4) for the field. The photon momentum in the LIF can be derived from the formalism in Section 3 of GH94, or by manipulation of the differential form of the trajectory equation in Eq. (A.1).

The result is

$$\mathbf{k}_{GR} = \frac{\varepsilon}{\Psi_b\sqrt{1-\Psi}}\left\{\sqrt{\Psi_b^2 - \Psi^2(1-\Psi)}\,\hat{r} + \Psi\sqrt{1-\Psi}\,\hat{\theta}\right\} \quad , \qquad (4.11)$$

which can be simply inferred from Eq. (A1) of Harding, Baring & Gonthier [1997]. From this, one can form the angle δ_e for the initial angle of the photon momentum relative to the radial direction, via $\sin\delta_e = |\mathbf{k}_{GR} \times \hat{r}|/|\mathbf{k}_{GR}| = \Psi_e\sqrt{1-\Psi_e}/\Psi_b$, a result that is the first identity in Eq. (4.7). Forming a cross product between the photon momentum and the field vectors, it follows that

$$\sin\theta_{kB} \equiv \frac{|\mathbf{k}_{GR} \times \mathbf{B}_{GR}|}{|\mathbf{k}_{GR}|.|\mathbf{B}_{GR}|} = \frac{B^{\hat{\theta}}}{B}\left[1 - (1-\Psi)\frac{\Psi^2}{\Psi_b^2}\right]^{1/2} - \frac{B^{\hat{r}}}{B}\frac{\Psi(1-\Psi)^{1/2}}{\Psi_b} \quad , \qquad (4.12)$$

an expression that is also routinely obtained by rearranging Eq. (37) of Gonthier & Harding [1994]. Inserting the forms for the field components, elementary manipulations yield

$$\sin\theta_{kB} = \frac{\sqrt{\Psi_b^2 - \Psi^2(1-\Psi)} - \Psi\sqrt{1-\Psi}\,\xi(\Psi)\,\cot\theta}{\Psi_b\,\sqrt{1 + [\xi(\Psi)]^2\cot^2\theta}} \qquad (4.13)$$

Insertion of the form for Ψ_b in Eq. (4.7) quickly reveals that when $\Psi = \Psi_e$, this expression yields $\sin\theta_{kB} = 0$. Using the fact that $\Psi^2(1-\Psi)$ is an increasing function for $0 < \Psi < 2/3$, and that $\xi(\Psi)$ is a more modestly declining function of Ψ on the same interval, it is routinely established that $\sin\theta_{kB}$ increases as r increases from the emission radius, i.e. Ψ drops below Ψ_e. Numerical comparisons of our computations of $\sin\theta_{kB}$ and the effective pair threshold $2/\sin\theta_{kB}$ with panels (a) and (b) of Fig. 5 of GH94 were performed, yielding excellent agreement. In the flat spacetime limit $\Psi_e \ll 1$, $\Psi_b \approx \Psi_e/\sin\delta_e \approx \Psi/\sin(\delta_e - \beta)$ can be deduced using Eq. (3.5), and then

it is straightforward to demonstrate that Eq. (4.13) reduces to Eq. (3.8).

Finally, we will need to change our integration variable from s to Ψ. In the LIF, the path length is related to the coordinate transit time: $ds^2 = (1 - \Psi)c^2 dt^2$ in the Schwarzschild case. Equivalently, the path length can be connected to the radial and angular (equatorial) contributions to the Schwarzschild metric via $ds^2 = dr^2/(1 - \Psi) + r^2 d\theta^2$. The two forms are equivalent, yielding the proper time interval $d\tau^2 = 0$ for light-like propagation. Employing Eq. (18) of GH94, or equivalently taking the derivative of Eq. (8.7.2) of Weinberg [1972], yields an expression for $dt/d\Psi$ for the photon's transit along its trajectory, essentially formulae for Shapiro delay. Assembling these pieces one quickly arrives at the change of variables

$$\frac{ds}{r_e} = -\frac{\Psi_e \, \Psi_b \, d\Psi}{\Psi^2 \sqrt{(1 - \Psi) \left\{ \Psi_b^2 - \Psi^2(1 - \Psi) \right\}}} \quad . \tag{4.14}$$

The optical depth integration for the case of including general relativity then takes the form

$$\tau(\Psi) = r_e \, \Psi_e \int_\Psi^{\Psi_e} \frac{\mathcal{R}(\omega, \, \sin\theta_{\mathrm{kB}}, \, B_{GR}) \, \Psi_b \, d\Psi_r}{\Psi_r^2 \sqrt{(1 - \Psi_r) \left\{ \Psi_b^2 - \Psi_r^2(1 - \Psi_r) \right\}}} \quad , \tag{4.15}$$

where the arguments of the scaled quantum pair creation rate $\mathcal{R}$ are given by Eqs. (4.1), (4.5) and (4.13). With this construct, we can formally define the attenuation length L as in Harding, Baring & Gonthier [1997] and Baring & Harding [2001] via

$$\tau\left(\Psi_L\right) = 1 \quad ; \quad s\left(\Psi_L\right) = L \quad . \tag{4.16}$$

When $\Psi_e \ll 1$, Eq. (4.15) is equivalent to the flat spacetime evaluation in Eq. (3.6).

It should be noted that we have also attempted comparisons between our work and Harding, Baring & Gonthier [1997] and Baring & Harding [2001]. Despite the agreement between our geometry and attenuation coefficient calculations and those presented in Gonthier & Harding [1994], our computations (for example, attenuation lengths like those in Fig. 4.1) differ from those presented in Harding, Baring & Gonthier [1997] by 20-30%. We continue to search for an explanation for these discrepancies, but for the present, all we can say is that we have checked our work thoroughly against both GH94 and the $\Psi_e \rightarrow 0$ flat spacetime limit, and we believe our results to be robust.

As a further additional note, when considering emission originating from the last open field line, it is important to take into account the decreased polar cap size resulting from the reshaping of the magnetic field in curved spacetime. Equation (27) in GH94 represents the correct form of the polar cap angle. This correction is used in computing the dotted lines in Fig. 4.3, and in the minimum altitude determinations in Fig. 4.4.

Figures 4.1 and 4.2 show the attenuation lengths computed for curved spacetime at two different magnetic fields. Eq. 4.16 defines L; this is approximately the distance that a photon of a given energy will travel from its emission point (here, restricted to the neutron star surface) before converting to an electron-positron pair. The curves turn up to infinity at the escape energy. In the first plot, the magnetic field is low, and so we see that although the attenuation lengths differ for the Erber and B88

attenuation coefficients, the escape energies are similar, as expected from parallels with Fig. 3.2. The second plot shows that, also as expected, the difference between the threshold-corrected attenuation lengths and the Erber asymptotic attenuation lengths increases dramatically as we approach the critical magnetic field.

The escape energies calculated with general relativistic effects are shown in Fig. 4.3 as a function of emission colatitude and emission altitude. The dotted lines indicate the escape energy along the last open field line for two different pulsar periods. At low altitudes, the expected trend of $\varepsilon_{\rm esc} \propto h^{7/2}$ is realized along the last open field line curves. To find a minimum altitude for emission, one would find the point along the last open field line curve where $\varepsilon_{\rm esc} = E_{cutoff}$. That point will lie along the r_e curve corresponding to the minimum radius.

Fig. 4.4 shows these minimum radii for the 47 pulsars in the first Fermi catalog [Abdo et al., 2010a], plus eight pulsars discovered in blind searches that were not included in the catalog [Saz Parkinson et al., 2010]. These minimum altitudes are calculated using the cutoff energies published in the catalog paper, which are not the highest energy photons detected from the source, but are close to the energy where the νF_ν is at a maximum, modulo a factor that depends on the power-law spectral index below the cutoff. Millisecond pulsars and a few other pulsars with relatively low cutoff energies are not constrained at all by this technique; their "minimum radii" are actually inside the neutron star. In the case of millisecond pulsars, their magnetic fields are too low for magnetic pair creation to play a significant role in

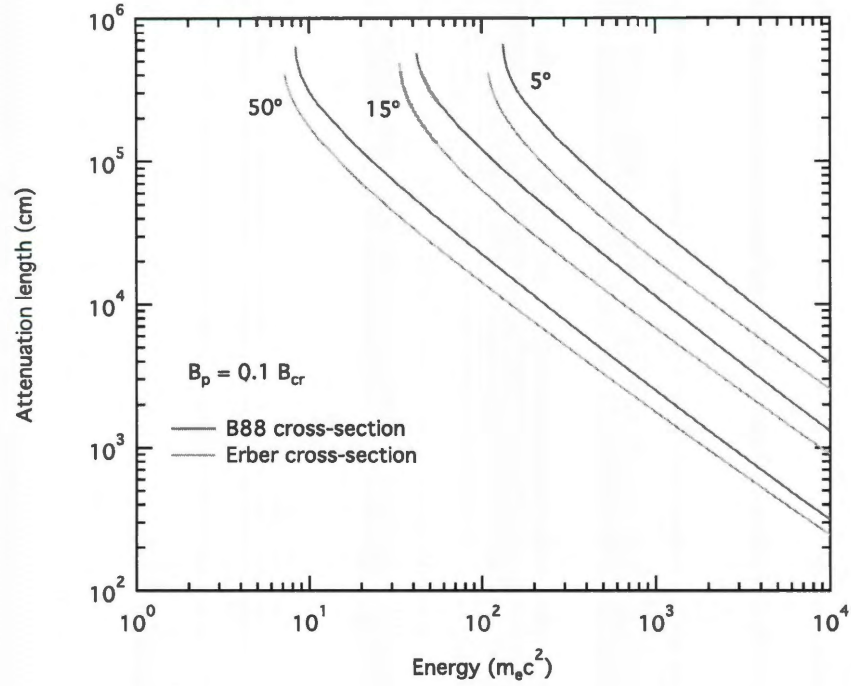photon propagation in their magnetospheres.

Figure 4.1 : Attenuation lengths for photons emitted at colatitudes of 5, 10, and 50 degrees, for a neutron star with surface polar magnetic field of $0.1B_{cr}$. These represent the quantity L, defined in Eq. (4.16) for curved spacetime and Eq. (3.1) for flat spacetime. Green curves show the attenuation length for the Erber attenuation coefficient of Eqs. (2.1) and (2.2); red curves show the attenuation length for the threshold-corrected attenuation coefficient in Eq. (2.3). The curves turn up and go to infinity at the escape energy.
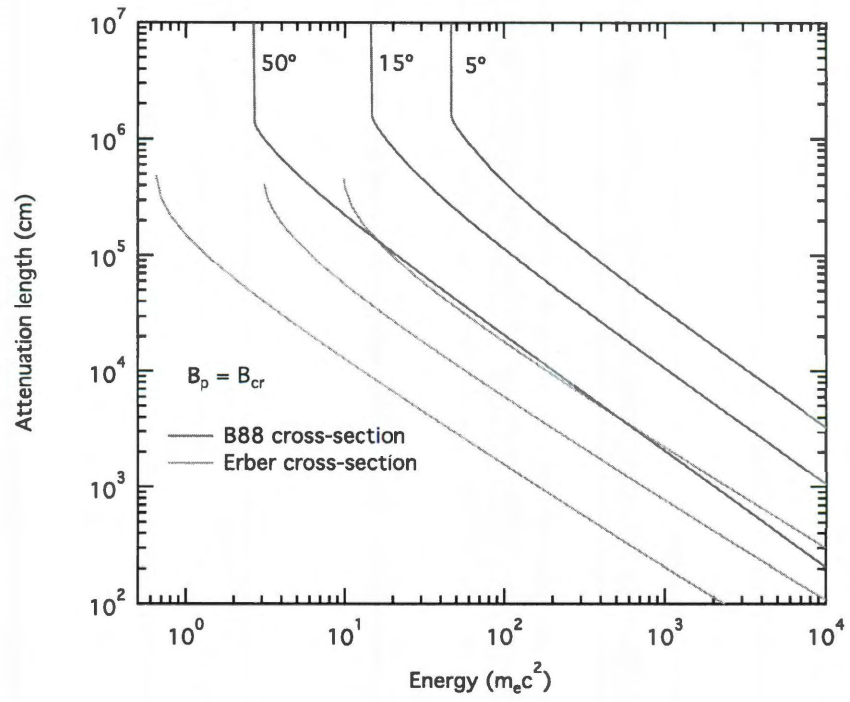
Figure 4.2 : Same as Fig. 4.1, but for a surface polar magnetic field of B_{cr}. Note that the difference between the Erber asymptotic and the Baring (1988) threshold-corrected curves increases sharply as the magnetic field increases.
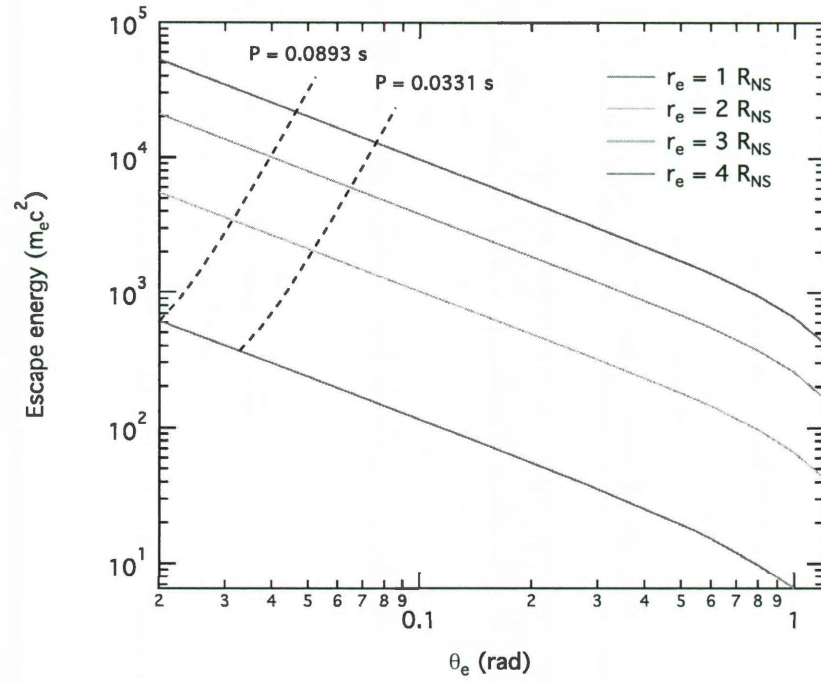
Figure 4.3 : Escape energies in curved spacetime for multiple radii of emission, as a function of emission colatitude. The two dotted curves pick out the last open field line for pulsars with periods of 0.033 s (Crab) and 0.089 s (Vela).
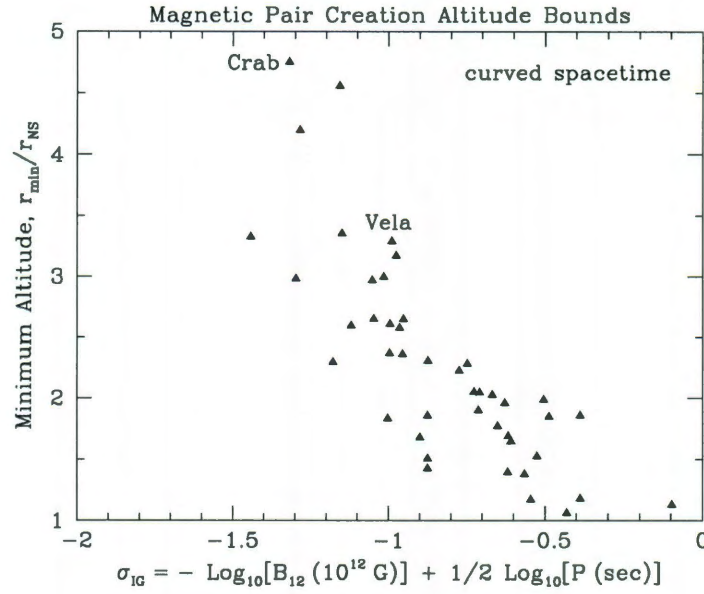
Figure 4.4 : Minimum emission radii for the 47 pulsars in the first Fermi catalog [Abdo et al., 2010a], plus 8 blind search pulsars from Saz Parkinson et al. [2010]. The minimum radius in neutron star radii is plotted against the log of $\sqrt{P}/B_{12}$, which is the dependence suggested in Baring [2004] from a semi-empirical fit to accommodate the influences of GR on ε_{esc}. These minimum radii are found by solving $\tau(r_e, \varepsilon_c) = 1$ for r_e, using the cutoff energies measured by Fermi for ε_c [Abdo et al., 2010a], and assuming that emission takes place on the last open field line. If the same calculation is done for the VERITAS detection of the Crab pulsar at 120 GeV, we get a minimum altitude of $15R_{NS}$ for the 120 GeV photons.

Chapter 5

Conclusions

In this work, we have calculated single-photon pair creation transparency conditions for neutron star magnetospheres, both for flat and curved spacetime. We calculate optical depths for arbitrary photon emission points in neutron star magnetospheres, in the special case where photons are emitted parallel to the magnetic field. Emission parallel to the magnetic field is expected because electrons that emit curvature radiation γ-rays have such high Lorentz factors that all the photons will be subject to very strong relativistic beaming. This has allowed us to present attenuation lengths, minimum altitudes of emission for a given energy, and escape energies for a given emission altitude.

Where prior results for the same calculation are available, we generally match them well. In Fig. 3.2, we show the agreement between our work and the corresponding calculation of flat spacetime escape energies in Chang, Chen, & Ho [1996]. The general relativistic calculation has resulted in partial agreement with previous calculations (including Gonthier & Harding [1994], Harding, Baring & Gonthier [1997], and Baring & Harding [2001]).

The main outcome of this work is a set of analytic and semi-analytic results that can greatly simplify the computation of magnetic pair creation opacities. These approximations can be applied to any emission altitude and most colatitudes, and may

prove useful in calculating pair multiplicities for pulsar wind nebula applications.

Our minimum altitudes are one of the few constraints available on the emission location in γ-ray pulsars with a single peak, and they have the advantage of being a physics-based constraint that is not solely dependent on the geometry of the emitting region. The minimum emission altitudes that we calculate from magnetic pair creation are far below those obtained from pulse profile fitting with slot gap or outer gap models, which are typically $r_{min} \sim 0.1 R_{LC} - R_{LC} \sim 100 R_{NS}$ for two-peaked pulsars. As such, they are not tremendously useful constraints on these curvature-radiation-based models. Nor are they expected to apply to millisecond pulsars, where the surface magnetic fields are too low for magnetic pair creation opacity to be significant. Thus, the magnetic pair creation calculations are expected to be most relevant to single-peaked pulsars and to questions about pulsar pair luminosities.

However, the geometric calculations we have done will be used again when we move on to investigating $\gamma - \gamma$ attenuation. If one photon in this interaction is a thermal x-ray from the neutron star surface, the pair creation energy threshold requires the other photon to be a GeV γ-ray. This natural energy dependence may better explain the observed GeV band turnovers. Because $\gamma - \gamma$ attenuation lacks the strong magnetic field dependence of single-photon magnetic pair creation, it occurs at much higher altitudes, and will provide a direct connection to slot gap and outer gap models.

Bibliography

Abdo, A. A. et al. 2009, Science, **325**, 840.

Abdo, A. A. et al. 2009, ApJ, **696**, 1084.

Abdo, A. A. et al. 2010, ApJS, **187**, 460.

Abdo, A. A. et al. 2010, ApJ, **713**, 154.

Abdo, A. A. et al. 2011, ApJ, in press, eprint `http://arxiv.org/abs/1107.4151`

Aleksić, J. et al. 2011, ApJ, **742**, 43.

Aliu, E. et al. 2008, Science, **322**, 1221.

Aliu, E. et al. 2011, Science, **334**, 69.

Arons, J. 1983, ApJ, **266**, 215.

Atwood, W. B. et al. 2006, ApJ, **652**, 49.

Baier, V. N. & Katkov, V. M. 2007, Phys. Rev. D, **75**, 073009.

Baring, M. G. 1988, MNRAS, **235**, 79.

Baring, M. G. 1991 A&A **249**, 581.

Baring, M. G. & Harding, A. K. 2001, ApJ, **547**, 929.

Baring, M. G. 2004, Adv. Space Research, **33**, 552.

Baring, M. G. & Harding, A. K. 2007, Ap&SS, **308**, 109.

Chang, H.-K., Chen, K. & Ho., C. 1996, A&AS, **120**, 81.

Cheng, K. S., Ho, C. & Ruderman, M. A. 1986, ApJ, **300**, 500.

Chiang, J. & Romani, R. W. 1994, ApJ, **436**, 754.

Daugherty, J. K. & Harding A. K., 1982, ApJ, **252**, 337.

Daugherty, J. K. & Harding, A. K. 1983, ApJ **273**, 761.

Daugherty, J. K. & Harding, A. K. 1996, ApJ, **458**, 278.

de Jager, O. C. 2007, ApJ, **658**, 1177.

Deutsch, A. 1955, Ann. d'Astrophys., **18**, 1.

Dyks, J. & Rudak, B. 2003, ApJ, **598**, 1201.

Erber, T. 1966, Rev. Mod. Phys., **38**, 626.

Gonthier, P. L. & Harding, A. K. 1994, ApJ, **425**, 767.

Harding, A. K., Baring, M. G. & Gonthier, P. L. 1997, ApJ, **476**, 246. (HBG97)

Harding, A. K. & Muslimov, A. G. 2004, Ap&SS, **297**, 63.

Harding, A. K. 2007, in *363-Heraeus-Seminar on Neutron Stars and Pulsars*, ed. W. Becker, eprint http://arxiv.org/abs/0710.3517

Harding, A. K. et al. 2011, in *2011 Fermi Symposium proceedings*, in press, http://arxiv.org/abs/1111.0828

Hirotani, K. 2011, ApJ, **733L**, 49.

Ho, C., Epstein, R. I., & Fenimore, E. E. 1990, ApJ, **348**, L25.

Johnson, T. J., Harding, A. K., & Venter, C. 2011, in *2011 Fermi Symposium proceedings*, http://arxiv.org/abs/1110.5476

Kalapotharakos, K., Kazanas, D., Harding, A. K. & Contopoulos, I. 2011, ApJ, submitted. arXiv:1108.2138

Kassim, N. E. & Lazio, T. J. W. 1999, ApJ, **527L**, 101.

Klepikov, N. V. 1954, Zh. Eksp. Theor. Fiz., **26**, 19.

Lee, K. J. et al. 2010, MNRAS, **405**, 2103.

Li, J., Spitkovsky, A., & Tchekhovskoy, A. 2011, ApJ, submitted. arXiv:1107.0979

Liu, Q. Z., van Paradijs, J. & van den Heuvel, E. P. J. 2006, A&A, 455, 1665L and http://heasarc.nasa.gov/W3Browse/all/hmxbcat.html

Malofeev, V. M. & Malov, O. I. 1997, Nature, **389**, 697.

Manchester, R. N., Hobbs, G. B., Teoh, A. & Hobbs, M. 2005, ApJ, **129**, 1993. and http://www.atnf.csiro.au/people/pulsar/psrcat/

Misner, C. W., Thorne, K. S. & Wheeler, J. A. 1973, *Gravitation* (W. H. Freeman and Co., San Francisco)

Muslimov, A. G. & Harding, A. K. 2004, ApJ, **606**, 1143.

Pechenick, K. R., Ftaclas, C. & Cohen, J. M. 1983, ApJ, **274**, 846.

Pierbattista, M., Grenier, I. A., Harding, A. K., & Gonthier, P. L. 2010, in *2009 Fermi Symposium proceedings*, http://arxiv.org/abs/1002.0324

Razzano, M. & Harding, A. K. 2007, in *The First GLAST Symposium*, eds. S. Ritz, P. F. Michelson & C. Meegan (AIP Conf. Proc. 921) p. 413.

Romani, R. W. 1996, ApJ, **470**, 469.

Ruderman, M. A. & Sutherland, P. G. 1975, ApJ, **196**, 51.

Saz Parkinson, P. M. et al. 2010, ApJ, **725**, 571.

Schwinger, J. 1951, Phys. Rev., **82**, 664.

Shapiro, S. L. & Teukolsky, S. A. 1983, *Black Holes, White Dwarfs, and Neutron Stars: The Physics of Compact Objects* (Wiley & Sons, New York)

Shearer, A., O'Connor, P., & Tuairisg, S. O. 2006, in *Proceedings of the 232nd Symposium of the International Astronomical Union*, ed. P. A. Whitelock, M. Dennefeld, & B. Leibundgut. Cambridge: Cambridge University Press, 2006., pp.281-285

Sokolov, A. A. & Ternov, I. M. 1968, Synchrotron Radiation, (Pergamon Press, Oxford).

Story, S. A., Gonthier, P. L., & Harding, A. K. 2007, ApJ, **671**, 713.

Sturrock, P. A. 1971, ApJ, **164**, 529.

Takata, J., Shibata, S., Hirotani, K., & Chang, H.-K. 2006, MNRAS, **366**, 1310.

Toll, J. S. 1952, Ph.D. Thesis, Princeton University.

Tsai, W.-Y. & Erber, T. 1974, Phys. Rev. D, **10**, 492.

Wang, R. & Hirotani, K. 2011, ApJ, **736**, 127.

Wasserman, I. & Shapiro, S. L. 1983, ApJ, **265**, 1036.

Watters, K. P. et al. 2009, ApJ, **695**, 1219.

Weinberg, S. 1972, *Gravitation and Cosmology: Principles and Applications of the General Theory of Relativity* (Wiley & Sons, New York).

Zavlin, V. E. 2007, in *363-Heraeus-Seminar on Neutron Stars and Pulsars*, ed. W. Becker, eprint http://arxiv.org/abs/astro-ph/0702426

Zhang, B. & Harding, A. K. 2000, ApJ, **532**, 1150.

Appendix A

Approximating the Photon Trajectory Curvature Integral

The following approximation was derived by Dr. Baring to simplify the computation of curved spacetime optical depths by eliminating the need to perform a double integral. Figures and numerical results were calculated by me.

The photon trajectory in curved spacetime is defined by colatitude θ expressed as an integral over the propagation altitude parameter $\Psi = r_s/r$, where r_s is the neutron star's Schwarzschild radius. The angle in Eq. (11) of GH94 is the difference between the angle (in the local inertial frame) of the photon momentum vector to the radial vector at the point of emission, and the angle of the photon trajectory to the local radial vector at a point defined by Ψ; it relates to θ as follows:

$$\theta(\Psi) \equiv \theta_e + \Delta\theta = \theta_e + \int_{\Psi}^{\Psi_e} \frac{d\Psi_r}{\sqrt{\Psi_b^2 - \Psi_r^2(1 - \Psi_r)}} \quad . \tag{A.1}$$

Since $\Psi \leq \Psi_e$ in this construction, as the photon propagates out from the star, then the change in colatitude $\Delta\theta$ is necessarily positive as the altitude r increases. Also, $\Psi_b = r_s/b$ expresses the general relativistic impact parameter b for the unbound photon path.

Computation of the trajectory using numerical integration is expensive in terms of time, particular for repeated applications in Monte Carlo simulations of magnetospheric cascades, so it is expedient to derive an analytic approximation to the integral

in Eq. (A.1). Using manipulations outlined in Chapter 17 of Abramowitz & Stegun (1965), this integral can be expressed in terms of elliptic functions. Such a step does not facilitate its evaluation, since the parameter Ψ_e/Ψ_b is not necessarily small, a condition that would render series expansion of elliptic functions more amenable. In our neutron star cases, $\Psi_e \lesssim 0.4$ is generally realized, and this suggests a series expansion in this parameter. To effect such, we have designed an expansion algorithm (not unique) that is motivated by the flat spacetime limit $\Psi_e \to 0$ of the integral. Define

$$\rho_f \;=\; \sqrt{\Psi_b^2 - \Psi_r^2} \quad , \quad \rho_c \;=\; \sqrt{\Psi_b^2 - \Psi_r^2(1 - \Psi_r)} \tag{A.2}$$

as flat and curved spacetime forms, respectively, of the denominator of the integrand of the trajectory integral. A Taylor series expansion for $\rho_c/\rho_f = \sqrt{1 + \Psi_r^3/\rho_f^2}$ can be developed in the generally small parameter Ψ_r^3/ρ_f^2. Note that this parameter is not much less than unity for near-surface, equatorial cases. This protocol results in a series expansion in Ψ_b for the integral:

$$\Delta\theta \;=\; \int_{\Psi}^{\Psi_e} \frac{d\Psi_r}{\rho_f} \left\{ 1 - \frac{\Psi_r^3}{2\rho_f^2} + \frac{3\Psi_r^6}{8\rho_f^4} - \frac{5\Psi_r^9}{16\rho_f^6} + \frac{35\Psi_r^{12}}{128\rho_f^8} \right\} + O\left(\Psi_e^5\right) \quad . \tag{A.3}$$

Now define the scaled parameters

$$\Upsilon \;=\; \frac{\Psi}{\Psi_b} \quad , \quad \Upsilon_e \;=\; \frac{\Psi_e}{\Psi_b} \quad . \tag{A.4}$$

The integrals in Eq. (A.3) are all analytically tractable, and yield a useful analytic approximation for the photon trajectory:

$$\Delta\theta \;\approx\; \Delta\theta_{\mathrm{app}} \;\equiv\; \left[\arcsin v - \Psi_b\, f_1(v) + \Psi_b^2\, f_2(v) - \Psi_b^3\, f_3(v) \right]_{\Upsilon}^{\Upsilon_e} \quad , \tag{A.5}$$

when retaining only the first four terms in the integrand of Eq. (A.3). Here

$$
\begin{aligned}
f_1(v) &= \frac{2 - v^2}{2\sqrt{1 - v^2}} - 1 \\
f_2(v) &= \frac{15}{16} \arcsin v - \frac{v\left(15 - 20v^2 + 3v^4\right)}{16\left(1 - v^2\right)^{3/2}} \\
f_3(v) &= \frac{128 - 320v^2 + 240v^4 - 40v^6 - 5v^8}{48(1 - v^2)^{5/2}} - \frac{8}{3}
\end{aligned}
\qquad (A.6)
$$

This provides an alternative to the Beloborodov (2002) approximation. As constructed, for small arguments v, the functions employed in the approximation scale as $f_n(v) \propto v^{1+3n}$. This regime is sampled for $\Psi_b \gg 1$, the low impact parameter cases appropriate for circumpolar colatitudes. Accordingly, the series implied by extension of Eq. (A.5) to higher order terms is nicely convergent even when Ψ_b is large.

For photon emission from the neutron star surface, with $\Psi_e \approx 0.4$, this approximation for the transit in colatitude is accurate to better than 0.1% at all subsequent altitudes for emission colatitudes $\theta_e \lesssim \pi/4$. Raising the altitude of emission, i.e. reducing Ψ_e below 0.1 substantially improves this. This level of precision is entirely suitable for the pertinent pulsar parameter space, where footpoint colatitudes are usually inferior to $\theta_f \lesssim 30°$. To illustrate this, in Fig. A.1 we plot the fractional precision $|\Delta\theta_{app}/\Delta\theta - 1|$ of the approximation in Eq. (A.5) relative to the exact integral in Eq. (A.1), as a function of Ψ for different colatitudes θ_e and altitudes Ψ_e representative of the locales sampled in the pair attenuation calculations. Given an emission altitude parameter Ψ_e, the emission colatitude θ_e can then be used to define the impact parameter Ψ_b in Eq. (4.7). The precision clearly is degraded at

high colatitudes, though is always better than 1% for the colatitudes illustrated. Yet, because the general relativistic curvature is diminished at higher emission altitudes, the range of colatitudes θ_e yielding a given level of precision increases as Ψ_e declines. To retain 0.1% precision, it is best to restrict use of the approximation to field line footpoint colatitudes $\theta_f \lesssim 45°$.
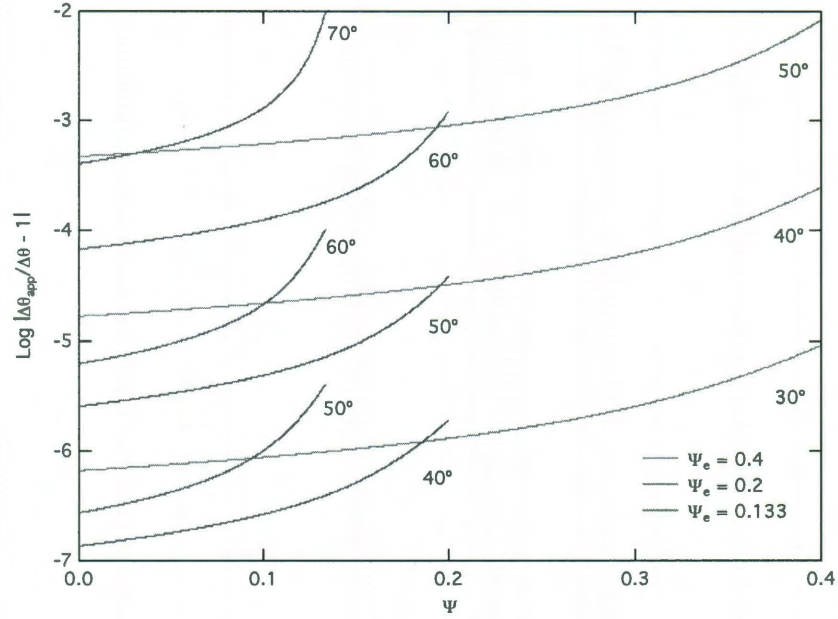
Figure A.1 : The fractional precision $|\Delta\theta_{\mathrm{app}}/\Delta\theta - 1|$ of the approximation in Eq. (A.5) to the full trajectory integral in Eq. (A.1) for photon propagation in curved space-time. Three groups of curves, color-coded, are illustrated for altitude parameters $\Psi_e = 0.4, 0.2, 0.133$, as marked, corresponding to emission at the neutron star surface and at two and three stellar radii. The range of altitudes $0 \leq \Psi \leq \Psi_e$ spans from the emission locale all the way out to infinity. Within each group are three curves for emission colatitudes θ_e, as labelled, illustrating how the precision of the approximation improves nearer the magnetic axis.